

1 **Influence of Synoptic Pattern and Low-Level Wind Speed on**
2 **Intensity and Diurnal Variations of Orographic Convection in Summer over Pearl**
3 **River Delta, South China**

4
5 **Xiaona Rao¹, Kun Zhao¹, Xingchao Chen², Anning Huang¹, Ming Xue¹,**
6 **Qinghong Zhang³, and Mingjun Wang¹**

7 ¹Key Laboratory of Mesoscale Severe Weather/MOE and School of Atmospheric Sciences,
8 Nanjing University, Nanjing, China, and State Key Laboratory of Severe Weather and Joint
9 Center for Atmospheric Radar Research of CMA/NJU, Beijing, China

10 ²Department of Meteorology and Atmospheric Science, and Center for Advanced Data
11 Assimilation and Predictability Techniques, The Pennsylvania State University, University Park,
12 Pennsylvania

13 ³Department of Atmospheric and Oceanic Sciences, School of Physics, Peking University,
14 Beijing, China.

15
16
17 Corresponding author: Kun Zhao (zhaokun@nju.edu.cn)

18
19 **Key Points:**

- 20 • The spatial distributions and diurnal variations of summer convective features over South
21 China under different synoptic patterns.
22 • Inland orographic convection is dominated by synoptic pattern with prevailing
23 southwesterly winds within the lower troposphere.
24 • Orographic convection is controlled by both the terrain thermal effects and the dynamic
25 forcing with the increase of wind speed.
26

27
28
29
30
31
32
33
34
35
36
37
38
39
40
41
42
43
44

Abstract

Based on five years of operational Doppler radar data, the influences of atmospheric synoptic patterns and low-level prevailing wind speed on the intensity and diurnal variations of summer orographic convection occurrence frequencies over Pearl River Delta (PRD), South China have been investigated. Results show that the inland orographic convection and rainfall generally occurs under synoptic pattern characterized with the prevailing southwesterly wind within the lower troposphere. The summer orographic convection over the mountains in northeastern PRD is not only controlled by the orographic thermal conditions but also the dynamic forcing with the increase of wind speed. Owing to the strong windward mechanical lifting and moisture transport associated with the strong ambient onshore winds, the number of convection occurrences characterized by a dominant diurnal afternoon peak occurs much more frequently in the high-wind-speed days. While due to the weak orographic mechanical lifting and moisture supply in the low-wind-speed days, the number of convection occurrences in the afternoon decreases considerably and two comparable peaks occur in the afternoon and early morning. The nighttime peak in the low-wind-speed days is mainly attributed to the nocturnal acceleration of the low-level southwesterly wind associated with the inertial oscillation and the corresponded enhanced windward lifting effects.

45 **1. Introduction**

46 As one of the three biggest population and economic zones in China, South China is also a
47 climatological rainfall center during summer (Luo et al., 2013). Frequent heavy rainfall and
48 associated floods bring loss of life and property damages, and urban inundation over South
49 China almost every year (Luo et al., 2017; H. Wang et al., 2014). Based on three years' radar
50 observations, X. Chen et al. (2014) demonstrated that convection over South China occurs most
51 frequently along the southern coast and the windward slope of the inland northeastern
52 mountainous area during the warm season (May-September). The spatial distribution of
53 convection roughly matches the accumulated precipitation spatial pattern, while convective
54 rainfall accounts for more than 45% of the total rainfall during warm season over South China
55 (X. Chen et al., 2014). Recent studies have suggested that diurnal cycles of rainfall and
56 convection over South China exhibit pronounced regional and intra-seasonal variations (G. Chen
57 et al., 2018; X. Chen et al., 2014; X. Chen et al., 2015; Jiang et al., 2017). Morning rainfall is
58 dominant over offshore regions because of the surface convergence between the northerly land
59 breeze and the prevailing southerly low-level monsoonal wind (G. Chen et al., 2018; X. Chen et
60 al., 2016; X. Chen et al., 2015). The rainfall and convection over the inland northeastern
61 mountainous area exhibits two diurnal peaks. The primary peak in the afternoon is associated
62 with the solar heating effect, whereas the secondary peak during midnight to the early morning is
63 closely related to the nocturnal acceleration of southwesterly boundary layer flow (X. Chen et
64 al., 2015). Further studies suggested that both the background wind and moisture can influence
65 the intensity and diurnal variations of rainfall over the coastal areas over South China (X. Chen
66 et al., 2019; X. Chen et al., 2017; Du & Rotunno, 2018). The low-level monsoonal wind speed is
67 the main factor controlling the diurnal variability of monsoon convection over South China (X.

68 Chen et al., 2017). However, few studies have conducted for the influences of low-level wind
69 speed on the inland orographic rainfall center over PRD, South China.

70 The role of large-scale wind speed on the orographic convection has been extensively
71 investigated and revealed in previous studies. Tian and Parker (2002) investigated the orographic
72 effects on mesoscale boundary layer convection under different wind speeds through a series of
73 idealized 2D numerical experiments; they found that the strong ascents and descents on both
74 sides of the hill pose a more important impact on convection than the terrain thermal effects as
75 the wind speed increases. Using an explicitly resolving cloud model, Miglietta and Rotunno
76 (2009) explored the response of the along-ridge-average precipitation to the topography and the
77 varying ambient atmosphere. Results have shown that under the conditions with relatively
78 weaker environmental wind speed (2.5 m s^{-1}), the cold-air outflow due to the convection
79 propagates farther upstream and induces new upstream convective cells, and the stationary
80 rainfall formation over the mountain ridge is prevented. However, for larger values of U (10, 20
81 m s^{-1}), the quasi-stationary convective cells and rainfall occur along the windward slope of the
82 mountain without significant cold pool.

83 By using the long term TRMM (Tropical Rainfall Measuring Mission) observations, Sobel
84 et al. (2011) suggested that the diurnal cycle of precipitation over small islands is stronger over
85 the Maritime Continent than that over the Caribbean. It is because the ambient wind over the
86 Maritime Continent is weaker than that of the Caribbean. S. Wang and Sobel (2017) conducted
87 idealized cloud-permitting simulations to examine the precipitating convection over small islands
88 as a function of large-scale wind speed. Results indicated that the large-scale winds notably
89 influence the diurnal cycles of rainfall over small tropical islands. The thermally forced sea-
90 breeze-related convection dominates when the large-scale wind is weak, whereas mechanically

91 forced convection is pronounced when the large-scale wind is enhanced. Based on observations
92 from the Caribbean island of Dominica, transition between thermally and mechanically forced
93 orographic convection are studied. Smith et al. (2012) showed that precipitation over Dominica
94 is sensitive to trade wind speed with a transition from thermally to mechanically triggered
95 convection as the wind speed increases. Diurnally varying thermal convection is dominant and
96 the strongest ascent occurs along the mountain ridge and the leeward side under the low wind
97 speed conditions ($U < 5 \text{ m s}^{-1}$). However, under strong trades ($U > 7 \text{ m s}^{-1}$), convection driven
98 by topography mechanically forcing occurs with the strongest updrafts over the windward
99 slopes. By comparing observations from the Dominica Experiment field campaign with
100 numerical simulations, Nugent et al. (2014) suggested that thermally driven convection is present
101 with the high mountaintop surface temperature and divergence above the island under weak
102 winds. However, topography lifting over the windward slope and leeside plunging flow are
103 dominant under strong winds, and enhanced ventilation as well as cloudiness over the windward
104 slopes reduce the mountaintop surface temperature.

105 Previous studies also examined the diurnal cycles of precipitation and/or convection over
106 South China during different periods of warm season (G. Chen et al., 2009; X. Chen et al., 2014;
107 X. Chen et al., 2015; Jiang et al., 2017). However, there are various weather systems even in a
108 certain period (usually divided by month). Besides, earlier studies mainly focused on the
109 transition from thermal forced to mechanical forced convection as the wind speed increases.
110 However, the influences of synoptic patterns combined with wind speeds on the diurnal variation
111 of orographic convection over PRD, South China are still unclear and need to be deeply revealed
112 and understood. Based on five years of operational Doppler radar observations at Guangzhou,
113 China, this study firstly examines the spatial and temporal characteristics of summer convection

114 over PRD, South China under typical synoptic patterns. Then the influence of low-level ambient
115 wind speed on the intensity and diurnal variability of inland orographic convection occurrence
116 frequencies and related physical mechanisms are also investigated.

117 The rest of the paper is organized as follows: data and methodology are introduced in
118 section 2. Section 3 gives the results of the classification of synoptic patterns over South China.
119 Spatial distributions and diurnal variations of the summer convection over PRD under typical
120 synoptic patterns and different ambient wind speeds are presented in section 4. In section 5, the
121 possible mechanisms related to the influence of low-level ambient wind speed on the orographic
122 convection occurrence frequencies and diurnal variability are explored. Summary and
123 conclusions are given in section 6.

124 **2. Data and Methodology**

125 **2.1 Radar Data and Data Processing**

126 The radar data and processing procedure used in this study are similar to those used in X.
127 Chen et al. (2014). The observed data for radar climatology were collected from China's
128 Weather Surveillance Doppler-1998 radar at Guangzhou (GZRD in Figure 1), operated by the
129 China Meteorological Administration (CMA). Similar to the WSR-88D radars of the United
130 States, the S band (10 cm wavelength) GZRD, with a 1° beam width, were operated in the
131 VCP21 (volume coverage pattern 21) scanning mode. There are nine elevations from 0.5° to
132 19.5° in the VCP21 mode (Crum et al., 1993). To maintain a calibration precision of 1 dB,
133 reflectivity of every volume scan was calibrated by using internally generated test signals. The
134 radar reflectivity data possess a range resolution of 1 km and a 230 km maximum Doppler range.
135 The GZRD (113.355°E , 23.0039°N) is located in the center of South China coastal region. The
136 coverage area of the radar is characterized by a plain surrounded by mountains at moderate

137 height (400-800 m) on the northeast and the coastline to the south. The GZRD data during each
138 summer (June-August) of 2011-2015 is used to investigate the spatial distribution and diurnal
139 cycle of convection over the study region of PRD (shown by black square in Figure 1), South
140 China.

141 Following J. Zhang et al. (2004), the contaminated radar reflectivity caused by mountain,
142 sea clutters or ground was removed as well. Then the reflectivity data were bilinearly
143 interpolated onto constant altitude plan position indicator (CAPPI) in Cartesian coordinate
144 systems with $1 \text{ km} \times 1 \text{ km} \times 1 \text{ km}$ resolution (Mohr & Vaughan, 1979). The CAPPIs were
145 constructed every 6 minutes with horizontal coverage of $150 \text{ km} \times 150 \text{ km}$ and extended up to 15
146 km in the vertical direction. More details on the quality control and interpolation procedures can
147 be found in X. Chen et al. (2014). Following M. Chen et al. (2014), a convection day over PRD
148 region is defined based on the GZRD radar reflectivity $\geq 40 \text{ dBZ}$ with the coverage over 16 km^2
149 lasting at least 3 times in a day.

150 The convective-stratiform classification scheme in Steiner et al. (1995) is applied to the
151 GZRD 2.5 km altitude CAPPI reflectivity data. In this study, we focus on the convective
152 components. The grid points with a reflectivity $\geq 40 \text{ dBZ}$ are defined as convective grids in the
153 first step of the classification. And then the mean reflectivity within the 11 km radius of the
154 convective grids defined in the first step are calculated, and grid points with reflectivity exceed
155 the average value by a specific threshold (see Figure 7 in Steiner et al. (1995)) are labeled as
156 convective as well. Finally, the surrounding grid points within an intensity-dependent radius
157 (see Figure 6b in Steiner et al. (1995)) around each convective grid are also included as
158 convective area. Following Romatschke et al. (2010), a convective feature refers to contiguous
159 convective grid points at the 2.5 km height, extending vertically in each column and including all

160 grid points from the echo base to the echo top. The number of convection occurrences (CON
161 hereafter) is defined as the count that the grid point is covered by convective features. Based on
162 the coverage area and echo top height, the convective features are also divided into six
163 categories. Convective features with the coverage area larger than 400 km^2 , between 100 and 400
164 km^2 , and smaller than 100 km^2 are defined as large, medium and small convection, respectively
165 (Xu & Zipser, 2012). As was described in C.-Z. Zhang et al. (2006), convective features with 15
166 dBZ echo top height higher than 12 km, lower than 6 km are defined as deep, shallow
167 convection, respectively. Convective features of moderate depth have echo tops between 6 km
168 and 12 km. Spatial distributions and temporal variations of convective features especially under
169 different typical synoptic patterns and different ambient wind speeds are investigated in this
170 study.

171 After identifying convective and stratiform radar echoes, different Z-R relationships are
172 used to estimate convective and stratiform precipitation intensity at each grid, respectively. For
173 the convective components, relationship $Z = 300 R^{1.4}$ (X. Chen et al., 2014) is applied, whereas Z
174 $= 200 R^{1.6}$ (Marshall & Palmer, 1948) is adopted for stratiform rainfall. The total rainfall is the
175 sum of convective and stratiform precipitation.

176 **2.2 Synoptic Data**

177 Data from NCEP Final (FNL, see <https://rda.ucar.edu/datasets/ds083.2/>) operational global
178 analysis and National Oceanic and Atmospheric Administration (NOAA) Global Forecast
179 System (GFS, see <https://rda.ucar.edu/datasets/ds335.0/>) are also used to conduct objective
180 synoptic classification and investigate the large-scale environmental conditions respectively.
181 These reanalysis data have a horizontal resolution of $1^\circ \times 1^\circ$ (FNL) and $0.5^\circ \times 0.5^\circ$ (GFS) and both
182 are available at 00, 06, 12 and 18 UTC each day.

183 **2.3 Objective Synoptic Classification Method**

184 The obliquely rotated principal component analysis (PCA) in T-mode (PCT hereafter) is
 185 applied to the FNL reanalysis data to separate different synoptic patterns in this study. Compared
 186 with other synoptic classification methods, this method performs best because it is able to
 187 reproduce predefine dominant patterns embedded in the dataset and the classification results
 188 contain higher temporal and spatial stability and less sensitivity to pre-set parameters (Huth,
 189 1996a). This method could give more realistic and physically interpretable synoptic patterns
 190 (Compagnucci & Richman, 2008; Huth, 1996a; Huth et al, 2008). Based on the PCT method, Li
 191 et al. (2016) analyzed the long term trends of hail day frequency in mainland China and
 192 associated changes in the atmospheric circulation patterns.

193 Different from commonly used principal component analysis (S-mode PCA), PCA in T-
 194 mode arranges input data matrix for PCA process in a different way so that the columns of input
 195 matrix represent time observations while the rows refer to grid points. In order to attain more
 196 realistic and physically interpretable synoptic patterns, an oblique rotation based on Richman
 197 (1986) is applied to a few retained leading components after the PCA process. Finally, each day
 198 pattern is classified to the type for which it has the highest loading. The method is developed by
 199 an open source software package called cost733class within the framework of COST Action 733
 200 ‘Harmonisation and Applications of Weather Type Classifications for European Regions’
 201 (Philipp et al., 2016). More details about this method can refer to Huth (1996a, 1996b).

202 **2.4 Harmonic Analysis**

203 To reveal the diurnal variations of CON, the 24-h time series of CON are normalized by
 204 their daily mean according to $N(h) = \frac{CON(h) - CON_m}{CON_s}$, where h ranging from 0 to 23 indicates the
 205 local standard time (LST hereafter, LST=UTC+8). $CON_m = \frac{1}{24} \sum_{h=0}^{23} CON(h)$ refers to the daily

206 mean of CON, and $CON_s = \sqrt{\frac{1}{24} \sum_{h=0}^{23} (CON(h) - CON_m)^2}$ is the standard deviation of CON.

207 Then harmonic analysis (Dai, 2001; Wallace, 1975; Wu et al., 2018; Yin et al., 2009) is applied
 208 to the normalized 24-h time series of CON data to obtain the amplitudes and phases of
 209 convection diurnal and semi-diurnal cycles. The first two harmonic components are retained to
 210 represent the diurnal and semi-diurnal cycles:

$$211 \quad f(t) = \bar{f} + S_1(t) + S_2(t) + \text{residual} \quad (1)$$

$$212 \quad S_m(t) = C_m \times \cos\left(m \frac{2\pi}{24} t - \sigma_m\right) \quad (2)$$

$$213 \quad e_m = \frac{0.5C_m^2}{f_{var}} \quad (3)$$

$$214 \quad F_m = \frac{0.5C_m^2 \times (24-2-1)}{(f_{var}-C_m^2) \times 2} \quad (4)$$

215 where $m = 1, 2$ denotes the first (S_1) and second (S_2) harmonics and represent the diurnal and
 216 semi-diurnal harmonic, respectively. The higher-order harmonics of the variability of CON are
 217 included in the last term (residual) of Equation (1). \bar{f} is the daily mean value of CON. The $t =$
 218 1,2,3, ... ,24 represents each hour of a day ranging from 0000 to 2300 LST and $f(t)$ is the
 219 estimation of CON at each hour of a day. C_m and σ_m represent the amplitude and the phase of
 220 the m_{th} harmonic component, respectively. f_{var} is the total daily variance of CON values; e_m ,
 221 defined as the percentage of total diurnal variations explained by the m_{th} harmonic, is an index to
 222 evaluate the contribution of the m_{th} harmonic to total daily variance. Results show that S_1 and S_2
 223 can explain up to 90% of the total variance (see section 4.3), so the error induced by neglecting
 224 those higher-order harmonics in Equations (1) should be small. F_m can be calculated according to
 225 the definition in Equation (4). By comparing F_m with the inverse of the F distribution function
 226 with 2 and 21 degrees of freedom at significance level 0.9, the F-test is carried out to examine
 227 the significance of the harmonics (Benedetto, 1996; Wu et al., 2018; Yin et al., 2009).

228 The diurnal variations (diurnal and semi-diurnal cycles) described by the first two
229 harmonics under different wind speeds are then examined to investigate the wind speed's
230 influence on the diurnal variations of the orographic convection.

231 **3. Synoptic Patterns**

232 A summary of an objective classification of synoptic patterns during summer from 2011 to
233 2015 (460 days in total) is presented in this section. The spatial patterns of geopotential height at
234 925 hPa over South China (13°-33°N, 107°-132°E) are classified into nine types (named from
235 Type 1 to Type 9) using the PCT method. The nine synoptic patterns are ranked according to
236 their occurrence frequencies during the whole summer.

237 The corresponding geopotential heights and mean horizontal wind vectors at 925 hPa for
238 each synoptic pattern are shown in Figure 2. More than 65% of the 460 days for the nine
239 synoptic patterns is contributed by the typical synoptic patterns of Types 1 and 2 with the
240 prevailing southerly monsoon flow in PRD (the black box in each graph). The most frequent
241 occurrences of Type 1 (226 days, 49.1%) with the prevailing southwesterly monsoon flow in
242 PRD dominate the whole summer season with the highest occurrence frequencies in June. This
243 southwesterly wind is closely related to the high pressure-gradient between the Western Pacific
244 subtropical high (WPSH) located around 23°N and the monsoon trough located over Indochina
245 (not shown). The WPSH moves northward to 28°N while a low-pressure center is located
246 between Vietnam and Hainan Island in the Type 2 pattern. The axis of the pressure gradient
247 shifted in a northeast-southwest direction, resulting in a stronger southeasterly flow over the
248 PRD. The occurrence frequencies for the other seven patterns (Types 3-9) are much smaller than
249 those of Types 1 and 2. In the Types 3-9, the PRD is not under the influence of the prevailing

250 southerly monsoonal winds so we only focus on the cases with the synoptic patterns of Types 1
251 and 2 in this study.

252 Based on the definition of convection day in section 2.1, 381 days and 187 (71) days are
253 identified as convection days for the whole summer and Type 1 (Type 2) pattern, respectively.
254 Analysis of convection spatial distribution and diurnal variations follows are based on the
255 convection days.

256 **4. Spatial and Diurnal Variations of Convection over Pearl River Delta**

257 **4.1 Spatial Distributions and Diurnal Variations of the Convective Features and** 258 **Rainfall in Typical Synoptic Patterns**

259 From the radar climatology perspective, X. Chen et al. (2014) showed that the southern
260 coast and the windward slope of the northeastern mountainous area over South China are the two
261 hotspots of convective features during May to September. Figure 3a shows the spatial
262 distribution of the accumulated CON in summer during 2011-2015. The accumulated CON at
263 each grid point is counted as the total number of times that the grid point is recognized as
264 convective grid within the five summer seasons. By extending the radar observation from three
265 to five years (2011-2015), we find that the convective features occur most frequently along the
266 southern coast and the northeastern inland mountainous region during summer, which is
267 consistent with findings of X. Chen et al. (2014). The spatial pattern of accumulated total rainfall
268 based on the radar quantitative precipitation estimate (QPE) using the Z-R relationships is shown
269 in Figure 3b. The accumulated rainfall at each grid point is the sum of hourly rainfall during five
270 summer seasons. Similar to CON distribution, the northeastern inland mountainous area and
271 south coast are two hotspots of summer rainfall, and convective rainfall contributes about 80% of
272 total rainfall.

273 Figures 3c and e show the spatial distributions of the five summers' accumulated CON
274 corresponding to the synoptic patterns of Types 1 and 2, respectively. The CON corresponding to
275 the synoptic pattern of Type 1 exhibits two maximal centers with one located along the southern
276 coast and the other situated at the windward slope (low-level prevailing winds are close to
277 southwesterly and approximately perpendicular to the northeastern mountain ridges in Type 1) of
278 the inland mountainous area in northeastern PRD (R1 box in Figure 3c). The spatial distribution
279 of CON in Type 1 (Figure 3c) are similar to the spatial pattern of total CON in summer (Figure
280 3a). CON in the windward slope of northeastern mountains is higher than that in the south coast
281 area under the synoptic pattern of Type 1, while the south coastal area undergoes more
282 convection during the whole summer. It is probably because the low-level prevailing wind
283 direction over South China is almost southwesterly and roughly perpendicular to the northeastern
284 mountain ridges under the synoptic pattern of Type 1, resulting in much stronger orographic
285 mechanical lifting effect than that of the whole summer with southerly winds as an average. The
286 convection corresponding to the Type 2 synoptic pattern occurs more frequently along the coast
287 (Figure 3e). The spatial distributions of total rainfall under synoptic pattern of Types 1 and 2
288 (Figures 3d and f) approximately match those of CON. Precipitation is mainly concentrated on
289 the northeastern inland mountainous area and south coast (south coast) in synoptic pattern of
290 Type 1 (Type 2). Therefore, the spatial distributions of CON and rainfall over PRD are closely
291 related to the synoptic patterns. More than 60% of the total convection and rainfall in summer
292 over the northeastern mountainous area is contributed by those corresponding to the Type 1
293 synoptic pattern (Figure 4c). However, Type 2 synoptic pattern contributes more than 40% (less
294 than 15%) of convection and rainfall over offshore region (inland northeastern mountainous

295 region) (Figure 4d). So Type 1 is the dominant synoptic pattern in terms of the orographic
296 summer convection (and rainfall) over northeastern PRD.

297 The prevailing warm and moist low-level southerly flows over South China lead to a low
298 free convection level (X. Chen et al., 2014). Therefore, the orographic lifting effect is strong
299 enough to trigger convection on the windward slope. Various studies have indicated that the
300 characteristics and physical mechanisms of coastal enhanced rainfall and convection are closely
301 related to the surface friction and land-sea breeze (G. Chen et al., 2018; X. Chen et al., 2017; X.
302 Chen et al., 2015; Jiang et al., 2017).

303 Diurnal variation is an important basic feature of convection and rainfall. During the past
304 decade, diurnal cycles of convection and rainfall over South China have been extensively studied
305 through rain gauge, radar, and satellite data (G. Chen et al., 2018; G. Chen et al., 2013; X. Chen
306 et al., 2014; X. Chen et al., 2015; Luo et al., 2013; Xu & Zipser, 2011; Yuan et al., 2010; Zhou et
307 al., 2008). Results showed that the diurnal features of rainfall and convection exhibit strong
308 regional and intra-seasonal variability. The diurnal variations of convection over the inland
309 mountainous over South China are closely related to the diurnal variations of the summer
310 monsoonal wind. The diurnal variations of the inland orographic convection under the typical
311 synoptic pattern of Types 1 and 2 are examined below.

312 Figure 4a shows the diurnal variations of total CON (units: Num) accumulated at all grids
313 along the inland mountainous windward slope (R1 box in Figure 3c) under the synoptic patterns
314 of Type 1 and Type 2. Diurnal cycles of total rainfall over inland mountainous area in Types 1
315 and 2 are presented in Figure 4b. The CON and precipitation on the windward slope
316 corresponding to the Type 1 synoptic pattern exhibit two diurnal peaks, with the primary peak in
317 the early afternoon around 1400 LST, and the secondary peak in early morning (0400-0500

318 LST). Compared with the situations corresponding to the Type 1 synoptic pattern, the diurnal
319 cycle of CON and rainfall with the Type 2 synoptic pattern show a slightly delayed afternoon
320 peak (around 1500-1600 LST) and a much weaker morning peak (around 0500-0600 LST). The
321 pronounced afternoon peak is apparently related to the increases of local instability due to the
322 diurnal solar heating (Luo et al., 2013). X. Chen et al. (2015) also noted the secondary diurnal
323 peak in the early morning over the windward slope of northeastern mountains during Mei-Yu
324 season, which is likely due to the nocturnal acceleration and enhanced lifting on the windward
325 slope of southwesterly boundary layer flow.

326 In summary, the spatial distributions and diurnal cycles of precipitation under different
327 synoptic patterns basically match those of convection occurrences. In addition, the diurnal cycle
328 of convection shown in the current study is consistent with the rainfall diurnal cycles revealed by
329 the long-term satellite observations (X. Chen et al., 2019). Therefore, we only focus on
330 characteristics of convection occurrences under Type 1 synoptic pattern in following sections.

331 **4.2 Spatial Distributions of Convective Features under Different Wind Speeds in** 332 **Dominant Synoptic Pattern**

333 As mentioned earlier, X. Chen et al. (2017) showed that the low-level monsoonal wind
334 speed is a key factor influencing the diurnal variations of the rainfall over the coastal regions of
335 South China in Mei-Yu season. However, the influence of the monsoonal wind speed on the
336 diurnal variations of inland orographic convection remains unclear. In this section, we examine
337 the spatial distributions and diurnal cycles of the summer convection over the inland
338 mountainous region under different low-level prevailing wind speeds in the dominant Type 1
339 synoptic pattern which accounts for the most inland orographic convection during summer.

340 For the Type 1 synoptic pattern, the prevailing wind in the lower troposphere is close to
341 southwesterly on average. To investigate the impact of the wind speed on the diurnal cycles of
342 convection, we calculate the daily mean prevailing wind speed at 925 hPa over PRD region
343 (21.7°-24.35°N, 111.9°-114.75°E; the black square in Figure 1) for each convection day (total
344 number of 187 days) with the Type 1 synoptic pattern based on the 0.5°×0.5° GFS data. Then all
345 the 187 days are sorted according to the mean wind speed at 925 hPa. Finally, thirty percent days
346 corresponding to the Type 1 pattern with relatively stronger wind speeds higher than 6.5 m s⁻¹
347 (weaker wind speeds lower than 4.5 m s⁻¹) are defined as the high (low)-wind-speed days, while
348 the rest of (forty percent) days with wind speeds ranging from 4.5 to 6.5 m s⁻¹ are considered as
349 the moderate-wind-speed days. 56 high-wind-speed days, 56 low-wind-speed days and 75
350 moderate-wind-speed days are picked out for composite analysis of different wind speed ranges.

351 Figure 5d displays the monthly variation of the days with different wind speeds in summer.
352 The high-wind-speed and the moderate-wind-speed days occur more frequently in June and July
353 while relatively more low-wind-speed days appear in August. Figures 5a-c show the spatial
354 distribution of the daily mean CON under the high-wind speed, the moderate-wind-speed and the
355 low-wind-speed days, respectively. (For example, the daily mean CON in the high-wind-speed
356 days is defined as the accumulated CON of the high-wind-speed days at each grid divided by 56
357 days). It is clearly shown that the intensity and spatial pattern of daily mean CON vary with the
358 ambient low-level wind speed. Convection occurs most frequently during the high-wind-speed
359 days, and it exhibits two maximal centers with one situated along the south coast (mean CON >
360 12) and the other located on the windward slope of the northeastern mountains (mean CON ~9).
361 CON decreases to less than five along the coast in the moderate-wind-speed days, and the inland
362 mountain area experiences a relatively smaller decrease. CON along the south coast and on the

363 windward slope of the northeastern mountains is significantly reduced to less than four in the
364 low-wind-speed days. The south coastal convection over South China reduced as the ambient
365 wind speed decreases, consistent with previous studies (X. Chen et al., 2017; X. Chen et al.,
366 2014). At the high onshore wind speed, the coastal rainfall/convection is closely related to the
367 strong low-level convergence induced by the differential surface friction and the small hills at the
368 coast (X. Chen et al., 2017). However, the influence of wind speed on the diurnal variations of
369 northeastern orographic convection and associated mechanisms are still unclear and will be
370 analyzed in the below sections.

371 **4.3 Diurnal Cycle and Propagation of Convection in Different Wind Speeds Days of** 372 **the Dominant Synoptic Pattern**

373 The diurnal variations of 24-h time series' daily mean CON over the inland mountainous
374 windward slope (box R1 in Figure 3c) in different wind speeds days of Type 1 synoptic pattern
375 are presented in Figure 6a. Diurnal cycle of daily mean CON exhibits a dominant early afternoon
376 peak (around 1300-1400 LST) and a local maximum in the early morning around 0400-0600
377 LST in the high-wind-speed days. In the moderate-wind-speed days, the CON shows two diurnal
378 peaks with a primary peak in the early afternoon (around 1400-1500 LST) and a secondary one
379 in the early morning (around 0500-0600 LST). Compared with the moderate-wind-speed days,
380 the afternoon peak appears relatively later (1600-1700 LST) while the morning peak occurs
381 slightly earlier (0300-0400 LST) under the low-wind-speed conditions. In addition, the
382 amplitude of afternoon peak is much weaker, resulting in two comparable diurnal peaks in the
383 low-wind-speed days. CON in the afternoon decreases with declining wind speed. In particular,
384 the CON maximum in the afternoon under the high-wind-speed conditions is nearly 5 times of
385 that under the low-wind-speed conditions. We compare the differences in the CON between the

386 high-wind-speed and the low-wind-speed days in the following sections to reveal the influence
387 of wind speed on the diurnal variation and intensity of the inland orographic convection
388 occurrence frequencies.

389 To further quantify the differences in the CON diurnal variation between the high-wind-
390 speed and the low-wind-speed days, we adopt the harmonic analysis on the normalized 24-h time
391 series of the CON regionally averaged over the inland mountainous area for the high-wind-speed
392 and the low-wind-speed days. The results of the harmonic analysis are shown in Figures 6b and
393 c. The percentage of the variances explained by the diurnal harmonic (S1) and semi-diurnal
394 harmonic (S2) to the total variance are indicated by the blue number and the green number,
395 respectively. It shows that the sum of explained variance for the first two harmonics reaches
396 nearly 90% for both the high-wind-speed and the low-wind-speed days, suggesting that the sum
397 (yellow line in Figures 6b and c) of the first two harmonics explain the majority of the daily
398 variance. Differences can also be found for the CON diurnal variations with different wind
399 speeds. The first harmonic explains much more variance than the second one (79% vs. 10.4%) in
400 the high-wind-speed days. Only the first one reaches the 90% significance level for the F-test. In
401 the low-wind-speed days, the explained variance of the semi-diurnal harmonic is much larger
402 than the diurnal one (61.3% vs. 28.3%), and both harmonics are significant, indicating that the
403 CON corresponding to the high (low) -wind-speed days exhibits single afternoon peak (two
404 comparable morning and afternoon peaks).

405 All convective features under the high-wind-speed and the low-wind-speed conditions are
406 also divided into six categories according to the definition described in section 2.1. The diurnal
407 cycles of convective features with different sizes and vertical depths over the windward slope of
408 inland mountains (R1 box in Figure 3c) under different wind speeds conditions are also

409 compared in Figure 7. The convective features are mainly contributed by large (and/or deep and
410 moderate depth) convective features in the high-wind-speed days. In the low-wind-speed days,
411 the morning convection is mainly contributed by large (and/or deep) convective features. In the
412 afternoon, however, the occurrences of the convective features with large and medium size
413 (and/or with deep and moderate depth) are comparable, indicating that smaller convection is
414 more likely to occur in the afternoon under low-wind-speed conditions. In addition, the diurnal
415 cycle of occurrences of convective features varies with size and vertical depth. Large and deep
416 convection occurrences exhibit two diurnal peaks with the primary one in the early afternoon and
417 the secondary peak in the early morning both under the high-wind-speed and the low-wind-speed
418 conditions (solid red lines). As for convective features with medium size and moderate vertical
419 depth, there is only a dominant afternoon peak (dashed blue lines). In general, small-scale
420 convective activities are closely related to the afternoon solar heating effects and the
421 corresponding upward branch of mountain–plains solenoid. However, larger convective systems
422 are induced by both this afternoon thermal forced circulation and an enhanced orographic lifting
423 induced by the nocturnal enhancement of the low-level wind speed. As a result, the diurnal cycle
424 of larger convective systems shows a double peak pattern (Figure 7). The detailed physical
425 mechanisms will be discussed in section 5.

426 Spatial propagation is also another important characteristic of convection, daily Hovmöller
427 diagrams of the hourly averaged CON in the high-wind-speed and the low-wind-speed days are
428 shown in Figures 8a and b, respectively. These two Hovmöller diagrams are aligned along the
429 short dimension (black SW-NE arrow in Figure 3c, approximately from southwest to northeast
430 orientation) and averaged along the long direction (perpendicular to SW-NE arrow) of the R1
431 box in Figure 3c. In the high-wind-speed days, one dominant maximum can be seen in the early

432 afternoon (around 1200-1500 LST). Similar to the results of Miglietta and Rotunno (2009), the
433 high-CON region in the high-wind-speed days is quasi-stationary and can be found mainly over
434 the mountainous and windward regions. This convection hotspot in the afternoon is related to the
435 solar heating, which is more effective in triggering convection over the mountain slope area
436 when the mountainous elevated heating is favorable for the formation of upslope solenoidal
437 circulations (X. Chen et al., 2015).

438 In the low-wind-speed days, the CON exhibits two comparable diurnal peaks with one in
439 the early morning around 0300-0500 LST and the other in the afternoon around 1400-1700 LST
440 (Figure 8b). The high-CON centers are located over the mountain region and the adjacent plains
441 (see the terrain contour in the bottom of Figures 8a and b). The early morning convection
442 propagates from the mountainous area to the upstream lower plains area, with a propagating
443 speed about 6 m s^{-1} . This upstream propagation may be related to the cold-air outflow
444 propagating upstream (Miglietta & Rotunno, 2009). Dynamical pressure perturbations induced
445 by low-level wind maxima (C. C. Wang et al., 2015) as well as the thermally driven gravity
446 waves (Du & Rotunno, 2015, 2018) are also two possible mechanisms, and additional analyses
447 are necessary in the future.

448 **5. Possible Mechanisms Related to the Intensity and Diurnal Cycle of Orographic** 449 **Convection in Different Wind Speeds Days of the Dominant Synoptic Pattern**

450 Based on the GFS reanalysis data, the atmospheric thermodynamic and moisture conditions
451 under different low-level wind speeds of Type 1 synoptic pattern are analyzed in this section.
452 The possible mechanisms responsible for the influences of low-level wind speed on the inland
453 orographic convection are also discussed.

454

455 **5.1 Thermal Environment Conditions**

456 Mean surface temperature and wind fields of 925 hPa at 1400 and 0200 LST are shown in
457 Figure 9 for the high-wind-speed (Figures 9a and c) and the low-wind-speed days (Figures 9b
458 and d). Large diurnal variation of surface temperature mainly exists over land. However, the
459 temperature diurnal ranges over the ocean are relatively weaker due to much larger heat capacity
460 of ocean relative to land. In addition, in the high-wind-speed days, the mean temperature at 1400
461 LST over land in PRD is 3-4 K lower than that in the low-wind-speed days, which is likely
462 related to enhanced ventilation and cloud shading effects (Nugent et al., 2014). Consequently,
463 the land sea thermal contrast in the afternoon is much stronger during the low-wind-speed days
464 than that during the high-wind-speed days. The diurnal variations of thermally forced winds
465 induced by the land sea contrast are stronger and consequently harder to be reversed (X. Chen et
466 al., 2017) in the low-wind-speed days. As a result, the establishment time of the sea (or land)
467 breeze is earlier in the high-wind-speed days than that in the low-wind-speed days.

468 Figures 10 and 11 show the spatial distributions of convection inhibition energy (CIN) and
469 convection available potential energy (CAPE) at 1400 LST and 0200 LST under different wind
470 speeds and the differences between the high-wind-speed and low-wind-speed days. It is clearly
471 noted that the CIN over the northeastern mountains doesn't show obvious differences between
472 the high-wind-speed and the low-wind-speed days at 1400 LST (Figure 10e). While CIN in the
473 low-wind-speed days is larger than that in the high-wind-speed days at 0200 LST (Figure 10f),
474 which is associated with smaller CON in the morning under the low-wind-speed conditions
475 (Figure 6a). In addition, the CAPE over the northeastern mountainous area in the high-wind-
476 speed days is slightly smaller than that in the low-wind-speed days both at 1400 LST and 0200
477 LST (Figure 11). The less CAPE over R1 region at 1400 LST in the high-wind-speed days is

478 very likely because it was during or after the intense convective activity which occurs around
479 1100-1500 LST (Figure 8a). However, even after 1400 LST, the CON is still higher in the high-
480 wind-speed days. This suggests that the topography mechanical lifting effect should be an
481 important contributor as the ambient wind speed increases (Smith et al., 2012; S. Wang & Sobel,
482 2017).

483 **5.2 Diurnal Variations of Low-Level Environmental Flow**

484 Diurnal variations of environmental flows and associated impacts on the inland orographic
485 convection under the high-wind-speed and low-wind-speed days are discussed in this section.

486 The 925 hPa mean wind fields (vectors) at 1400 LST and 0200 LST in the high-wind-speed
487 (low-wind-speed) days are presented in Figures 9a and c (Figures 9b and d). In general, the mean
488 prevailing low-level winds are southwesterly to southerly with the much stronger wind speed
489 over ocean than that over land. Mean wind speed over PRD in the high-wind-speed days is
490 around 7 (8) m s^{-1} at 1400 LST (0200 LST). In the low-wind-speed days, mean wind speed over
491 PRD is about 1.5 m s^{-1} at 1400 LST and 3.5 m s^{-1} at nighttime (0200 LST), suggesting that the
492 prevailing wind speed is considerably increased at nighttime in the low-wind-speed days. The
493 nighttime acceleration of low-level winds can be seen more clearly by plotting the perturbation
494 wind at 0200 LST (Figures 9e and f), the daily mean at 925 hPa has been removed to highlight
495 the nighttime enhancement. It is shown that nighttime enhancement of low-level wind speed over
496 PRD in the high-wind-speed days is around 0.75 m s^{-1} (Figure 9e), only reaching 10% of the
497 daily mean wind speed (8 m s^{-1}) at 925 hPa. The deviated winds over PRD attains $\sim 1.25 \text{ m s}^{-1}$ at
498 0200 LST in the low-wind-speed days (Figure 9f), implying that the nocturnal acceleration of the
499 low-level prevailing winds reaches approximately 40% of the daily mean wind speed (3.3 m s^{-1})
500 at 925 hPa.

501 To further investigate the diurnal variations of low-level winds, the perturbation wind fields
502 at cross sections along the dashed line A-B (southwest-northeast orientation) in Figure 5a at
503 0800, 1400, 2000 and 0200 LST are shown in Figure 12. The average prevailing winds below
504 800 hPa over PRD are southwesterly to southerly (not shown). From daytime to nighttime, the
505 horizontal southwesterly wind speeds (shading) over the plains and mountain slopes (22.5 °N-
506 23.5 °N) are enhanced from surface to 900 hPa with strongest acceleration occurring at 925 hPa
507 ($\sim 1.2 \text{ m s}^{-1}$), leading to the strengthened windward dynamic lifting (arrows between 23.2 °N-24
508 °N) in the low-wind-speed days (Figure 12h). Consequently, CON increases and results in the
509 early morning peak in the low-wind-speed days. However, in the high-wind-speed days, the
510 nocturnal acceleration of the prevailing low-level southwesterly winds is weaker (only $\sim 0.5 \text{ m s}^{-1}$
511 1) and are found at higher levels (above 950 hPa) (Figure 12d). The horizontal southwesterly
512 wind speeds decrease with the magnitude up to 1.0 m s^{-1} below 975 hPa at 0200 LST. The low-
513 level southwesterly winds are enhanced below 975 hPa at 0800 LST (Figure 12a), indicating that
514 the nocturnal southwesterly winds can also be enhanced but later than that of the low-wind-speed
515 days. As a result, the time that CON reaches a local maximum (~ 0500 LST) under the high-
516 wind-speed conditions is 2-3 hours later than the morning peak in the low-wind-speed days
517 (~ 0300 LST; Figure 6a). The horizontal southwesterly wind speeds and windward lifting weaken
518 from surface to 900 hPa in the low-wind-speed days at 1400 LST (Figure 12f). However, in the
519 high-wind-speed days, the intensified horizontal southwesterly winds below 975 hPa leads to
520 strengthened windward mechanical lifting effect in the afternoon.

521 The close relationship between the nighttime low-level southwesterly jet in the boundary
522 layer and convection over South China has been well recognized in previous studies (X. Chen et
523 al., 2015; Du & Chen, 2018, 2019), in which the nocturnal boundary layer jet can be mainly

524 attributed to the inertial oscillation (Blackadar, 1957). According to the inertial oscillation theory,
525 the amplitude of nighttime acceleration is proportional to the diurnally varying turbulent mixing
526 and frictional effect in the boundary layer (Blackadar, 1957; Du & Rotunno, 2014). Figure 13
527 shows the diurnal variations of the GFS planetary boundary layer height (HPBL hereafter) over
528 PRD region. The HPBL is about 1100-1300 m along the line A-B in the early afternoon (1400
529 LST) during the high-wind-speed days (Figure 13a). In the low-wind-speed days (Figure 13c),
530 the HPBL is higher (1200-1500 m) with a local maximum (about 1500 m) located over the urban
531 area where the surface temperature is highest (Figure 9b). Such difference can be seen more
532 directly by comparing the HPBL difference between different wind speeds days (Figure 13e).
533 Generally, in the low-wind-speed days, the HPBL over the northeastern inland mountainous
534 region and adjacent urban area is about 200 m higher than that in the high-wind-speed days
535 (Figure 13e). At nighttime, however, the HPBL along the line A-B in the low-wind-speed days is
536 50-150 m lower when compared to that in the high-wind-speed days (Figure 13f), especially in
537 the urban area and the windward slope of the northeastern inland mountainous region (100-150
538 m lower). The larger day-night difference in the HPBL suggests that the diurnal variations of
539 turbulent mixing and frictional effect is stronger in the low-wind-speed days, which produces a
540 stronger nocturnal enhancement of the low-level prevailing southwesterly winds (Figure 12h).
541 The increase (reduction) of southwesterly wind speeds below 975 hPa at 1400 (0200) LST is
542 likely due to the sea (land) breeze is established earlier and advected far inland owing to the
543 strong prevailing ambient winds in the high-wind-speed days (X. Chen et al., 2017; Hu & Xue,
544 2016). However, to understand the specific mechanisms responsible for the differences in the
545 diurnal variations of low-level winds under different wind speeds, more studies are required in
546 the future.

547 **5.3 Impacts of Moisture Content in Boundary Layer**

548 X. Chen et al. (2017) suggested that the coastal rainfall of South China is not only
549 controlled by the ambient onshore wind speed but also sensitive to the incoming moisture
550 especially the moisture content in the boundary layer (0-1 km). The influences of the moisture
551 content transported by the low-level winds on the inland orographic convection under different
552 ambient wind speeds are also investigated here.

553 Firstly, the daily mean moisture fluxes in the boundary layer in the high-wind-speed (Figure
554 14a) and the low-wind-speed days (Figure 14b) are explored. The moisture fluxes is integrated
555 from surface to 900 hPa at each grid and calculated according to $\text{Flux} = \frac{1}{g} \int_{p_1}^{p_2} q \vec{V} dp$ (g , q , \vec{V} , p
556 are gravity acceleration, specific humidity, the horizontal velocity vector and pressure,
557 respectively; p_1 , p_2 are respectively the surface pressure and 900 hPa.). Moisture in the boundary
558 layer transported to PRD in the high-wind-speed days is more than twice of that in the low-wind-
559 speed days ($\sim 80 \text{ kg}\cdot\text{m}^{-1}\cdot\text{s}^{-1}$ vs. $\sim 30 \text{ kg}\cdot\text{m}^{-1}\cdot\text{s}^{-1}$), mainly caused by the much stronger low-level
560 prevailing winds.

561 The diurnal variations of net moisture fluxes into the inland mountainous region (defined as
562 the sum of the moisture fluxes in the four boundaries of dashed boxes in Figures 14a and b) are
563 shown in Figure 14c. The net moisture fluxes in the high-wind-speed days are higher than that in
564 the low-wind-speed days. Especially at 1400 LST, the net moisture fluxes in the high-wind-
565 speed days is around 8 times of that in the low-wind-speed days ($123 \text{ kg}\cdot\text{m}^{-1}\cdot\text{s}^{-1}$ vs. $15 \text{ kg}\cdot\text{m}^{-1}\cdot\text{s}^{-1}$).
566 However, the enhancement of moisture supply from daytime to nighttime in the low-wind-
567 speed days is stronger than that in the high-wind-speed days as a response to the more significant
568 nighttime enhancement of low-level prevailing winds.

569 Thus, the early morning peak of CON under the low-wind-speed conditions is believed to
570 be due to the enhanced low-level prevailing winds, upslope lifting, and moisture transport. The
571 prevailing wind speeds as well as associated windward lifting effects and moisture transport are
572 much stronger through the whole day in the high-wind-speed days, resulting in high CON. In
573 addition, the dominant peak of CON in the afternoon is due to the solar heating, abundant
574 moisture supply, and the enhanced windward mechanical lifting below 975 hPa at 1400 LST.
575 However, the much weaker mechanical windward forcing and net moisture fluxes at 1400 LST
576 result in the remarkable decrease of CON in the afternoon under the low-wind-speed conditions.

577 **6. Summary and Conclusions**

578 Complimentary to the previous study of X. Chen et al. (2017) who investigated the
579 influence of monsoonal wind speed and moisture content on the intensity and diurnal variations
580 of coastal rainfall over South China during Mei-Yu season, this study aims to reveal the
581 influence of the low-level monsoonal wind speed on the diurnal variations and intensity of inland
582 orographic convection occurrence frequencies over northeastern PRD, South China in summer.
583 In this paper, based on five years of operational weather radar observations and FNL reanalysis
584 data, the connection between the CON and the synoptic patterns is also examined by utilizing an
585 objective synoptic classification method called the T mode obliquely rotated principal
586 component analysis (PCT method). Main findings are shown as follows:

587 The climatic mean of the summer time CON and rainfall over PRD, South China exhibits
588 two maximal centers with one located along the southern coastline region and the other situated
589 over the northeastern mountainous regions. Additionally, about 80% of total summer
590 precipitation are contributed by convective rainfall. The low-level synoptic patterns over South
591 China are classified into nine types with PCT method by using the geopotential height at 925

592 hPa. Results show that the first two most frequent types (Type 1 49%, Type 2 17%) account for
593 up to 65%. Prevailing winds over PRD in synoptic pattern of Type 1 is close to southwesterly,
594 and the Type 2 pattern is featured by stronger southeasterly flows over PRD, South China.

595 Spatial distributions and diurnal variations of CON and rainfall are closely related to
596 synoptic patterns. The convection and rainfall corresponding to the synoptic pattern of Type 1
597 (2) occur more frequently in the northeastern inland mountains and southern coast (along the
598 southern coastline). The CON on the windward slope corresponding to the Type 1 synoptic
599 pattern exhibits two diurnal peaks with a primary early afternoon peak and a secondary early
600 morning peak. The CON in the synoptic pattern of Type 2 also displays similar double peaks.
601 Meanwhile, the convection and rainfall corresponding to Type 1 contributes more than 60% of
602 the inland orographic convection and rainfall during summer, indicating that Type 1 is the
603 dominant synoptic pattern for the inland orographic convection and rainfall center.

604 The prevailing low-level wind speed can also affect the intensity and diurnal variations of
605 orographic convection occurrence frequencies in the dominant synoptic pattern of Type 1. The
606 CON is much higher in the high-wind-speed days than that in the low-wind-speed days,
607 especially in the afternoon. The diurnal variation of CON shows a dominant early afternoon peak
608 around 1400 LST and a small increase in the early morning around 0400-0600 LST in the high-
609 wind-speed days, while the morning and afternoon peaks of CON become comparable in the
610 low-wind-speed days. The convective features are mainly contributed by large and/or deep
611 convective features in the high-wind-speed days. In contrast, smaller convection is more likely to
612 occur in the afternoon under the low-wind-speed conditions, and the reduction of CON in the
613 afternoon in the low-wind-speed days is mainly caused by the decrease of large convection. The
614 convection in the high-wind-speed days is mostly concentrated over the windward and

615 mountainous regions and is quasi-stationary. The morning orographic convection in the low-
616 wind-speed days exhibits an upstream propagation. This can be partly explained by the cold-pool
617 effect, pressure perturbations due to the low-level wind maximum and thermally forced gravity
618 waves.

619 The terrain thermal effects alone are not strong enough for the orographic convection
620 formation over PRD in summer and the topography mechanical forcing plays an important role
621 as well. Compared with the high-wind-speed days, the much warmer surface over the inland
622 regions leads to much larger land-sea thermal contrast in the low-wind-speed days at 1400 LST.
623 In addition, the afternoon CAPE in the high-wind-speed days is slightly smaller than that of the
624 low-wind-speed days, suggesting that the high CON in the high-wind-speed days is not only
625 determined by the thermal environment conditions and the mechanical forcing induced by
626 topography is very important. Relative to the low-wind-speed days, the moisture fluxes below
627 900 hPa are much stronger throughout the whole day in the high-wind-speed days. The net
628 moisture fluxes over the inland mountainous region at 1400 LST is about 8 times of that in the
629 low-wind-speed days. Under the high-wind-speed conditions, the combination of the strong
630 orographic mechanical lifting and the abundant moisture supply leads to high CON, especially
631 the large and/or deep convective features. Diurnal variation of the low-level prevailing winds
632 associated with the inertial oscillation leads to the nocturnal acceleration and daytime
633 deceleration of prevailing winds below 900 hPa under the low-wind-speed conditions.
634 Consequently, the prevailing southerly winds and windward mechanical lifting are strengthened
635 at nighttime, resulting in the early morning peak of CON in the low-wind-speed days. Under the
636 low-wind-speed conditions, afternoon convection (especially the large convective features) are
637 reduced considerably, which can be attributed to the weakened windward dynamic lifting effect

638 and moisture transport as well as more isolated convective features owing to the relative weak
639 ambient wind speeds in the afternoon. In addition, due to the weak dynamical lifting in the
640 afternoon under the low-wind-speed conditions, convection is mainly driven by thermal forcing
641 and takes more time to accumulated unstable energy. As a result, the afternoon peak of CON is
642 2-3 hours later than that in the high-wind-speed days. In the high-wind-speed days, the nighttime
643 enhancement of prevailing winds below 975 hPa is later than that of the low-wind-speed days,
644 and the local maximum of CON in the early morning is 2-3 hours later than the early morning
645 peak of the low-wind-speed days. The prevailing winds below 975 hPa is influenced by the sea
646 (land) breeze at 1400 (0200) LST in the high-wind-speed days, which may be explained as the
647 sea (land) breeze is established earlier and spread far inland under the high-wind-speed
648 conditions.

649 To understand the mechanism related to the diurnal variations of low-level winds under
650 different ambient wind speeds and the physical link between the prevailing wind speed and the
651 diurnal patterns of inland orographic convection, more studies based on dataset with higher
652 resolution as well as convection-permitting numerical sensitivity experiments are required in the
653 future.

654

655

656 **Acknowledgements:** We gratefully acknowledge Wen-Chau Lee from National Center for
657 Atmospheric Research, Boulder, CO, USA, Chuntao Liu from Texas A&M University and Yali
658 Luo from Chinese Academy of Meteorological Sciences for their valuable suggestions. We also
659 thank the editor and three reviewers for their comments that improved our paper. This work was
660 primarily supported by the National Key Research and Development Program of China (grant

661 number 2017YFC1501703) and the National Natural Science Foundation of China (grants
662 41475015, 41275031, 41322032), and the Open Research Program of the State Key Laboratory
663 of Severe Weather. We acknowledge Guangdong Meteorological Bureau for collecting and
664 archiving the radar data. The radar data and reanalysis data (FNL, GFS) are available at this
665 website (<https://pan.baidu.com/s/1DwaeJepGH0KHmkMa7vjN0w#list/path=%2F>).

666

667

668

669

670

671

672

673

674

675

676

677

678

679

680

681

682

683

684 **References**

- 685 Benedetto, J. J. (1996). *Harmonic analysis and applications* (Vol. 23): CRC Press.
- 686 Blackadar, A. K. (1957). Boundary layer wind maxima and their significance for the growth of nocturnal inversi
687 ons. *Bulletin of the American Meteorological Society*, 283-290.
- 688 Chen, G., Lan, R., Zeng, W., Pan, H., & Li, W. (2018). Diurnal Variations of Rainfall in Surface and Satellite Obse
689 rvations at the Monsoon Coast (South China). *Journal of Climate*, 31(5), 1703-1724. <https://journals.ametsoc.org/doi/abs/10.1175/JCLI-D-17-0373.1>
- 690 Chen, G., Sha, W., & Iwasaki, T. (2009). Diurnal variation of precipitation over southeastern China: 2. Impact o
691 f the diurnal monsoon variability. *Journal of Geophysical Research: Atmospheres*, 114(D21). <https://agupubs.onlinelibrary.wiley.com/doi/abs/10.1029/2009JD012181>
- 692 Chen, G., Sha, W., Sawada, M., & Iwasaki, T. (2013). Influence of summer monsoon diurnal cycle on moisture
693 transport and precipitation over eastern China. *Journal of Geophysical Research: Atmospheres*, 118(8), 31
694 63-3177. <https://agupubs.onlinelibrary.wiley.com/doi/abs/10.1002/jgrd.50337>
- 695 Chen, M., Wang, Y., Gao, F., & Xiao, X. (2014). Diurnal evolution and distribution of warm-season convective s
696 torms in different prevailing wind regimes over contiguous North China. *Journal of Geophysical Research:
697 Atmospheres*, 119(6), 2742-2763. <https://agupubs.onlinelibrary.wiley.com/doi/abs/10.1002/2013JD021145>
- 700 Chen, X., Zhang, F., & Jr., J. H. R. (2019). Modulations of the Diurnal Cycle of Coastal Rainfall over South China
701 Caused by the Boreal Summer Intraseasonal Oscillation. *Journal of Climate*, 32(7), 2089-2108. <https://journals.ametsoc.org/doi/abs/10.1175/JCLI-D-18-0786.1>
- 702 Chen, X., Zhang, F., & Zhao, K. (2016). Diurnal Variations of the Land–Sea Breeze and Its Related Precipitation
703 over South China. *Journal of the Atmospheric Sciences*, 73(12), 4793-4815. <https://journals.ametsoc.org/doi/abs/10.1175/JAS-D-16-0106.1>
- 704 Chen, X., Zhang, F., & Zhao, K. (2017). Influence of Monsoonal Wind Speed and Moisture Content on Intensity
705 and Diurnal Variations of the Mei-Yu Season Coastal Rainfall over South China. *Journal of the Atmospheric
706 Sciences*, 74(9), 2835-2856. <https://journals.ametsoc.org/doi/abs/10.1175/JAS-D-17-0081.1>
- 707 Chen, X., Zhao, K., & Xue, M. (2014). Spatial and temporal characteristics of warm season convection over Pea
708 rl River Delta region, China, based on 3 years of operational radar data. *Journal of Geophysical Research: A
709 tmospheres*, 119(22), 12,447-412,465. <https://agupubs.onlinelibrary.wiley.com/doi/abs/10.1002/2014JD021965>
- 710 Chen, X., Zhao, K., Xue, M., Zhou, B., Huang, X., & Xu, W. (2015). Radar-observed diurnal cycle and propagatio
711 n of convection over the Pearl River Delta during Mei-Yu season. *Journal of Geophysical Research: Atmosp
712 heres*, 120(24), 12557-12575. <https://agupubs.onlinelibrary.wiley.com/doi/abs/10.1002/2015JD023872>
- 713 Compagnucci, R. H., & Richman, M. B. (2008). Can principal component analysis provide atmospheric circulati
714 on or teleconnection patterns? *International Journal of Climatology: A Journal of the Royal Meteorological
715 Society*, 28(6), 703-726.
- 716 Crum, T. D., Alberty, R. L., & Burgess, D. W. (1993). Recording, Archiving, and Using WSR-88D Data. *Bulletin of
717 the American Meteorological Society*, 74(4), 645-788.
- 718 Dai, A. (2001). Global Precipitation and Thunderstorm Frequencies. Part II: Diurnal Variations. *Journal of Clim
719 ate*, 14(6), 1092-1111.
- 720 Du, Y., & Chen, G. (2018). Heavy Rainfall Associated with Double Low-Level Jets over Southern China. Part I: E
721 nsemble-Based Analysis. *Monthly Weather Review*, 146(11), 3827-3844. <https://journals.ametsoc.org/doi/abs/10.1175/MWR-D-18-0101.1>
- 722 Du, Y., & Chen, G. (2019). Heavy Rainfall Associated with Double Low-Level Jets over Southern China. Part II: C
723 onvection Initiation. *Monthly Weather Review*, 147(2), 543-565. <https://journals.ametsoc.org/doi/abs/10.1175/MWR-D-18-0102.1>
- 724 Du, Y., & Rotunno, R. (2014). A Simple Analytical Model of the Nocturnal Low-Level Jet over the Great Plains o
725 f the United States. *Journal of the Atmospheric Sciences*, 71(10), 3674-3683. <https://journals.ametsoc.org/doi/abs/10.1175/JAS-D-14-0060.1>
- 726
727
728
729
730
731
732

- 733 Du, Y., & Rotunno, R. (2015). Thermally Driven Diurnally Periodic Wind Signals off the East Coast of China. *Journal of the Atmospheric Sciences*, 72(7), 2806-2821. <https://journals.ametsoc.org/doi/abs/10.1175/JAS-D-14-0339.1>
- 734
- 735
- 736 Du, Y., & Rotunno, R. (2018). Diurnal Cycle of Rainfall and Winds near the South Coast of China. *Journal of the Atmospheric Sciences*, 75(6), 2065-2082. <https://journals.ametsoc.org/doi/abs/10.1175/JAS-D-17-0397.1>
- 737
- 738 Hu, X.-M., & Xue, M. (2016). Influence of Synoptic Sea-Breeze Fronts on the Urban Heat Island Intensity in Dallas-Fort Worth, Texas. *Monthly Weather Review*, 144(4), 1487-1507. <https://journals.ametsoc.org/doi/abs/10.1175/MWR-D-15-0201.1>
- 739
- 740
- 741 Huth, R. (1996a). An intercomparison of computer-assisted circulation classification methods. *International Journal of Climatology: A Journal of the Royal Meteorological Society*, 16(8), 893-922.
- 742
- 743 Huth, R. (1996b). Properties of the circulation classification scheme based on the rotated principal component analysis. *Meteorology and Atmospheric Physics*, 59(3), 217-233. journal article. <https://doi.org/10.1007/BF01030145>
- 744
- 745
- 746 Huth, R., Beck, C., Philipp, A., Demuzere, M., Ustrnul, Z., Cahynová, M., et al. (2008). Classifications of Atmospheric Circulation Patterns. *Annals of the New York Academy of Sciences*, 1146(1), 105-152. <https://nyaspubs.onlinelibrary.wiley.com/doi/abs/10.1196/annals.1446.019>
- 747
- 748
- 749 Jiang, Z., Zhang, D.-L., Xia, R., & Qian, T. (2017). Diurnal Variations of Presummer Rainfall over Southern China. *Journal of Climate*, 30(2), 755-773. <https://journals.ametsoc.org/doi/abs/10.1175/JCLI-D-15-0666.1>
- 750
- 751 Li, M., Zhang, Q., & Zhang, F. (2016). Hail Day Frequency Trends and Associated Atmospheric Circulation Patterns over China during 1960–2012. *Journal of Climate*, 29(19), 7027-7044. <https://journals.ametsoc.org/doi/abs/10.1175/JCLI-D-15-0500.1>
- 752
- 753
- 754 Luo, Y., Wang, H., Zhang, R., Qian, W., & Luo, Z. (2013). Comparison of Rainfall Characteristics and Convective Properties of Monsoon Precipitation Systems over South China and the Yangtze and Huai River Basin. *Journal of Climate*, 26(1), 110-132. <https://journals.ametsoc.org/doi/abs/10.1175/JCLI-D-12-00100.1>
- 755
- 756
- 757 Luo, Y., Zhang, R., Wan, Q., Wang, B., Wong, W. K., Hu, Z., et al. (2017). The Southern China Monsoon Rainfall Experiment (SCMREX). *Bulletin of the American Meteorological Society*, 98(5), 999-1013. <https://journals.ametsoc.org/doi/abs/10.1175/BAMS-D-15-00235.1>
- 758
- 759
- 760 Marshall, J. S., & Palmer, W. M. K. (1948). THE DISTRIBUTION OF RAINDROPS WITH SIZE. *Journal of Meteorology*, 5(4), 165-166. <https://journals.ametsoc.org/doi/abs/10.1175/1520-0469%281948%29005%3C0165%3ATDORWS%3E2.0.CO%3B2>
- 761
- 762
- 763 Miglietta, M. M., & Rotunno, R. (2009). Numerical Simulations of Conditionally Unstable Flows over a Mountain Ridge. *Journal of the Atmospheric Sciences*, 66(7), 1865-1885. <https://journals.ametsoc.org/doi/abs/10.1175/2009JAS2902.1>
- 764
- 765
- 766 Mohr, C. G., & Vaughan, R. L. (1979). An Economical Procedure for Cartesian Interpolation and Display of Reflectivity Factor Data in Three-Dimensional Space. *Journal of Applied Meteorology*, 18(5), 661-670.
- 767
- 768 Nugent, A. D., Smith, R. B., & Minder, J. R. (2014). Wind Speed Control of Tropical Orographic Convection. *Journal of the Atmospheric Sciences*, 71(7), 2695-2712. <https://journals.ametsoc.org/doi/abs/10.1175/JAS-D-13-0399.1>
- 769
- 770
- 771 Philipp, A., Beck, C., Huth, R., & Jacobbeit, J. (2016). Development and comparison of circulation type classifications using the COST 733 dataset and software. *International Journal of Climatology*, 36(7), 2673-2691. <https://rmets.onlinelibrary.wiley.com/doi/abs/10.1002/joc.3920>
- 772
- 773
- 774 Richman, M. B. (1986). Rotation of principal components. *Journal of climatology*, 6(3), 293-335.
- 775
- 776 Romatschke, U., Medina, S., & Jr., R. A. H. (2010). Regional, Seasonal, and Diurnal Variations of Extreme Convection in the South Asian Region. *Journal of Climate*, 23(2), 419-439. <https://journals.ametsoc.org/doi/abs/10.1175/2009JCLI3140.1>
- 777
- 778 Smith, R. B., Minder, J. R., Nugent, A. D., Storelvmo, T., Kirshbaum, D. J., Warren, R., et al. (2012). Orographic Precipitation in the Tropics: The Dominica Experiment. *Bulletin of the American Meteorological Society*, 93(10), 1567-1579.
- 779
- 780
- 781 Sobel, A. H., Burleyson, C. D., & Yuter, S. E. (2011). Rain on small tropical islands. *Journal of Geophysical Research: Atmospheres*, 116(D8). <https://agupubs.onlinelibrary.wiley.com/doi/abs/10.1029/2010JD014695>
- 782
- 783 Steiner, M., Houze, R. A., & Yuter, S. E. (1995). Climatological Characterization of Three-Dimensional Storm Structure from Operational Radar and Rain Gauge Data. *J.appl.meteor*, 34(34), 1978-2007.
- 784

- 785 Tian, W.-S., & Parker, D. J. (2002). Two-dimensional simulation of orographic effects on mesoscale boundary-l
786 ayer convection. *Quarterly Journal of the Royal Meteorological Society*, 128(584), 1929-1952. [https://rmet
788 s.onlinelibrary.wiley.com/doi/abs/10.1256/003590002320603476](https://rmet
787 s.onlinelibrary.wiley.com/doi/abs/10.1256/003590002320603476)
- 789 Wallace, J. M. (1975). Diurnal Variations in Precipitation and Thunderstorm Frequency over the Conterminous
790 United States. *Monthly Weather Review*, 103(5), 406-419. [https://journals.ametsoc.org/doi/abs/10.1175/
792 1520-0493%281975%29103%3C0406%3ADVIPAT%3E2.0.CO%3B2](https://journals.ametsoc.org/doi/abs/10.1175/
791 1520-0493%281975%29103%3C0406%3ADVIPAT%3E2.0.CO%3B2)
- 793 Wang, C. C., Kuo, H. C., Johnson, R. H., Lee, C. Y., Huang, S. Y., & Chen, Y. H. (2015). A numerical study of conv
794 ection in rainbands of Typhoon Morakot (2009) with extreme rainfall: roles of pressure perturbations with
795 low-level wind maxima. *Atmospheric Chemistry and Physics*, 15, 19(2015-10-06), 15(6), 8479-8523.
- 796 Wang, H., Luo, Y., & Jou, B. J.-D. (2014). Initiation, maintenance, and properties of convection in an extreme r
797 ainfall event during SCMREX: Observational analysis. *Journal of Geophysical Research: Atmospheres*, 119(2
798 3), 13,206-213,232. <https://agupubs.onlinelibrary.wiley.com/doi/abs/10.1002/2014JD022339>
- 799 Wang, S., & Sobel, A. H. (2017). Factors Controlling Rain on Small Tropical Islands: Diurnal Cycle, Large-Scale
800 Wind Speed, and Topography. *Journal of the Atmospheric Sciences*, 74(11), 3515-3532. [https://journals.a
802 metsoc.org/doi/abs/10.1175/JAS-D-16-0344.1](https://journals.a
801 metsoc.org/doi/abs/10.1175/JAS-D-16-0344.1)
- 803 Wu, Y., Huang, A., Huang, D., Chen, F., Yang, B., Zhou, Y., et al. (2018). Diurnal variations of summer precipitat
804 ion over the regions east to Tibetan Plateau. *Climate Dynamics*, 51(11), 4287-4307. journal article. [https://
806 doi.org/10.1007/s00382-017-4042-x](https://
805 doi.org/10.1007/s00382-017-4042-x)
- 807 Xu, W., & Zipser, E. J. (2011). Diurnal Variations of Precipitation, Deep Convection, and Lightning over and Eas
808 t of the Eastern Tibetan Plateau. *Journal of Climate*, 24(2), 448-465. [https://journals.ametsoc.org/doi/abs/
810 10.1175/2010JCLI3719.1](https://journals.ametsoc.org/doi/abs/
809 10.1175/2010JCLI3719.1)
- 811 Xu, W., & Zipser, E. J. (2012). Properties of deep convection in tropical continental, monsoon, and oceanic rai
812 nfall regimes. *Geophysical Research Letters*, 39(7). [https://agupubs.onlinelibrary.wiley.com/doi/abs/10.10
814 29/2012GL051242](https://agupubs.onlinelibrary.wiley.com/doi/abs/10.10
813 29/2012GL051242)
- 815 Yin, S., Chen, D., & Xie, Y. (2009). Diurnal variations of precipitation during the warm season over China. *Inter
816 national Journal of Climatology*, 29(8), 1154-1170.
- 817 Yuan, W., Yu, R., Chen, H., Li, J., & Zhang, M. (2010). Subseasonal Characteristics of Diurnal Variation in Summ
818 er Monsoon Rainfall over Central Eastern China. *Journal of Climate*, 23(24), 6684-6695. [https://journals.a
820 metsoc.org/doi/abs/10.1175/2010JCLI3805.1](https://journals.a
819 metsoc.org/doi/abs/10.1175/2010JCLI3805.1)
- 821 Zhang, C.-Z., Uyeda, H., Yamada, H., Geng, B., & Ni, Y. (2006). Characteristics of mesoscale convective systems
822 over the east part of continental China during the Meiyu from 2001 to 2003. *Journal of the Meteorologica
823 l Society of Japan. Ser. II*, 84(4), 763-782.
- 824 Zhang, J., Wang, S., & Clarke, B. (2004). P5. 4 WSR-88D reflectivity quality control using horizontal and vertical
reflectivity structure. Paper presented at the Proceedings of the 11th Conference on Aviation, Range and A
erospace Meteorology. IS.
- Zhou, T., Yu, R., Chen, H., Dai, A., & Pan, Y. (2008). Summer Precipitation Frequency, Intensity, and Diurnal Cy
cle over China: A Comparison of Satellite Data with Rain Gauge Observations. *Journal of Climate*, 21(16), 3
997-4010. <https://journals.ametsoc.org/doi/abs/10.1175/2008JCLI2028.1>

825 **Figure captions:**

826 Figure 1. The location of the Guangzhou radar (GZRD), together with the 150 km range
827 circle. The study region (Pearl River Delta) is marked by the black square (21.7°-24.35°N,
828 111.9°-114.75°E). Coastlines and provincial borders are shown by black lines. Shading denotes
829 orography (units: m).

830 Figure 2. The nine synoptic patterns (Type 1-Type 9) based on geopotential height at 925
831 hPa (shading, units: gpm) over South China in summer during 2011-2015. The number of days
832 for each pattern and their percentages are shown in the top left; the mean horizontal wind vectors
833 at 925 hPa are superimposed; black boxes represent Pearl River Delta region.

834 Figure 3. (left) Spatial distributions of accumulated number of convection occurrences
835 (CON, units: Num) (a) during 2011-2015 summer seasons, (c) under the synoptic pattern of Type
836 1, and (e) under the synoptic pattern of Type 2. (right: b, d, f) As in (left: a, c, e), but for
837 accumulated total rainfall based on radar QPE (units: mm). Black contours indicate orography of
838 150 m. Blue contours in (b) represent the percentage of convective rainfall to 5-yr total rainfall
839 during the whole summer at 80%. Note that the range of color bar in (a) or (b) is different from
840 that in (c, e) or (d, f).

841 Figure 4. Diurnal cycles of (a) total number of convection occurrences (CON, units: Num),
842 (b) accumulated total rainfall (QPE, units: mm) over inland mountainous region (indicated by R1
843 box in Figure 3c) for Types 1 and 2. (c) Percentage of Type 1 to the whole summer in total
844 number of convection occurrences (shading, units: %) and total rainfall (white contours: 60%).
845 (d) As in (c), but for Type 2, the black contours are 40%.

846 Figure 5. Spatial distributions of daily mean number of convection occurrences (units:
847 Num) in (a) the high-wind-speed days, (b) the moderate-wind-speed days, (c) the low-wind-

848 speed days. Black contours indicate orography of 150 m. (d) Monthly variation in occurrence
849 days of different wind speeds in Type 1. All daily mean wind speeds in Type 1 are divided into
850 12 intervals ranging from 0.5-1.5 m s⁻¹ to 11.5-12.5 m s⁻¹.

851 Figure 6. (a) Diurnal cycles of daily mean number of convection occurrences over inland
852 northeastern mountainous slope (R1 box in Figure 3c) (units: Num) under different wind speeds
853 days in Type 1. Observed normalized hourly mean number of convection occurrences (dots)
854 together with the fitted first (dashed blue curve), second (dashed green curve) harmonics and the
855 sum of the two harmonics (yellow curve) in (b) the high-wind-speed days, (c) the low-wind-
856 speed days in Type1. The percentages denoted by blue and green numbers represent the explain
857 variance of the first and second harmonic, respectively.

858 Figure 7. Diurnal variations of the convective features occurrence number over the inland
859 northeastern mountainous region (R1 box in Figure 3c). Convective features with different sizes
860 in (a) the high-wind-speed days and (b) the low-wind-speed days, and for convective features
861 with different depths in (c) the high-wind-speed days and (d) the low-wind-speed days.

862 Figure 8. Hovmöller diagrams of mean hourly number of convection occurrences in (a) the
863 high-wind-speed days, (b) the low-wind-speed days along direction SW-NE arrow and averaged
864 along the other direction (perpendicular to SW-NE arrow) of the R1 box in Figure 3c. Black
865 contour at the bottom of each panel represents the mean orography along SW-NE arrow.

866 Figure 9. Mean surface temperature (shading, units: °C) and mean horizontal wind vectors
867 (arrows) at 925 hPa at (a) 1400 LST, (c) 0200 LST; and (e) perturbation wind vectors (arrows)
868 and speeds (shading, units: m s⁻¹) at 0200 LST in the high-wind-speed days. (b, d, f) As in (a, c,
869 e), but for the low-wind-speed days. Dashed lines A-B indicate the line A-B in Figure 5a.

870 Figure 10. Mean surface convection inhibition energy (CIN, units: $\text{J}\cdot\text{kg}^{-1}$) over Pearl River
871 Delta region in the high-wind-speed days at (a) 1400 LST, (b) 0200 LST, and in the low-wind-
872 speed days at (c) 1400 LST and (d) 0200 LST; CIN of the high-wind-speed days minus the low-
873 wind-speed days at (e) 1400 LST, (f) 0200 LST. To facilitate comparison, CIN is multiplied by -
874 1. Black boxes corresponding to R1 box in Figure 3c represent the windward slope of
875 northeastern mountainous region. Black contours, from 100 to 1100 with 200 m intervals
876 indicate orography.

877 Figure 11. As in Figure 10, but for convection available potential energy (CAPE, units:
878 $\text{J}\cdot\text{kg}^{-1}$).

879
880 Figure 12. Perturbation wind vectors (arrows) at the cross section along the dashed line A-B
881 in Figure 5a and the perturbation wind component (shading, units: m s^{-1}) projected to the plane at
882 (a) 0800 LST, (b) 1400 LST, (c) 2000 LST, and (d) 0200 LST in the high-wind-speed days. (e)-
883 (h) As in (a)-(d), but for the low-wind-speed days. Vertical velocity is scaled by 10 for
884 visualization. Black shading on the bottom of each panel represents the interpolated topographic
885 profiles.

886 Figure 13. Mean GFS planetary boundary layer height (HPBL, units: m) over Pearl River
887 Delta region in the high-wind-speed days at (a) 1400 LST, (b) 0200 LST, and in the low-wind-
888 speed days at (c) 1400 LST and (d) 0200 LST; The HPBL of the high-wind-speed days minus
889 the low-wind-speed days at (e) 1400 LST, (f) 0200 LST. Black contours, from 100 to 1100 with
890 200 m intervals indicate orography. The dashed lines A-B indicate the location of the
891 corresponding vertical cross section presented in Figure 12.

892 Figure 14. Daily mean water vapor fluxes (units: $\text{kg}\cdot\text{m}^{-1}\cdot\text{s}^{-1}$) integrated from surface to 900
893 hPa in (a) the high-wind-speed days, (b) the low-wind-speed days. (c) Net moisture fluxes (units:
894 $\text{kg}\cdot\text{m}^{-1}\cdot\text{s}^{-1}$) into the budget region of the inland northeastern mountainous area (22° - 23°N , 113° -

895 114.5°E, indicated by the dashed box in (a, b)) at four times in the high-wind-speed and the low-
896 wind-speed days. Brown contours in (a, b), from 150 to 1150 with 250 m intervals indicate
897 orography.

898

899

Figure 1.

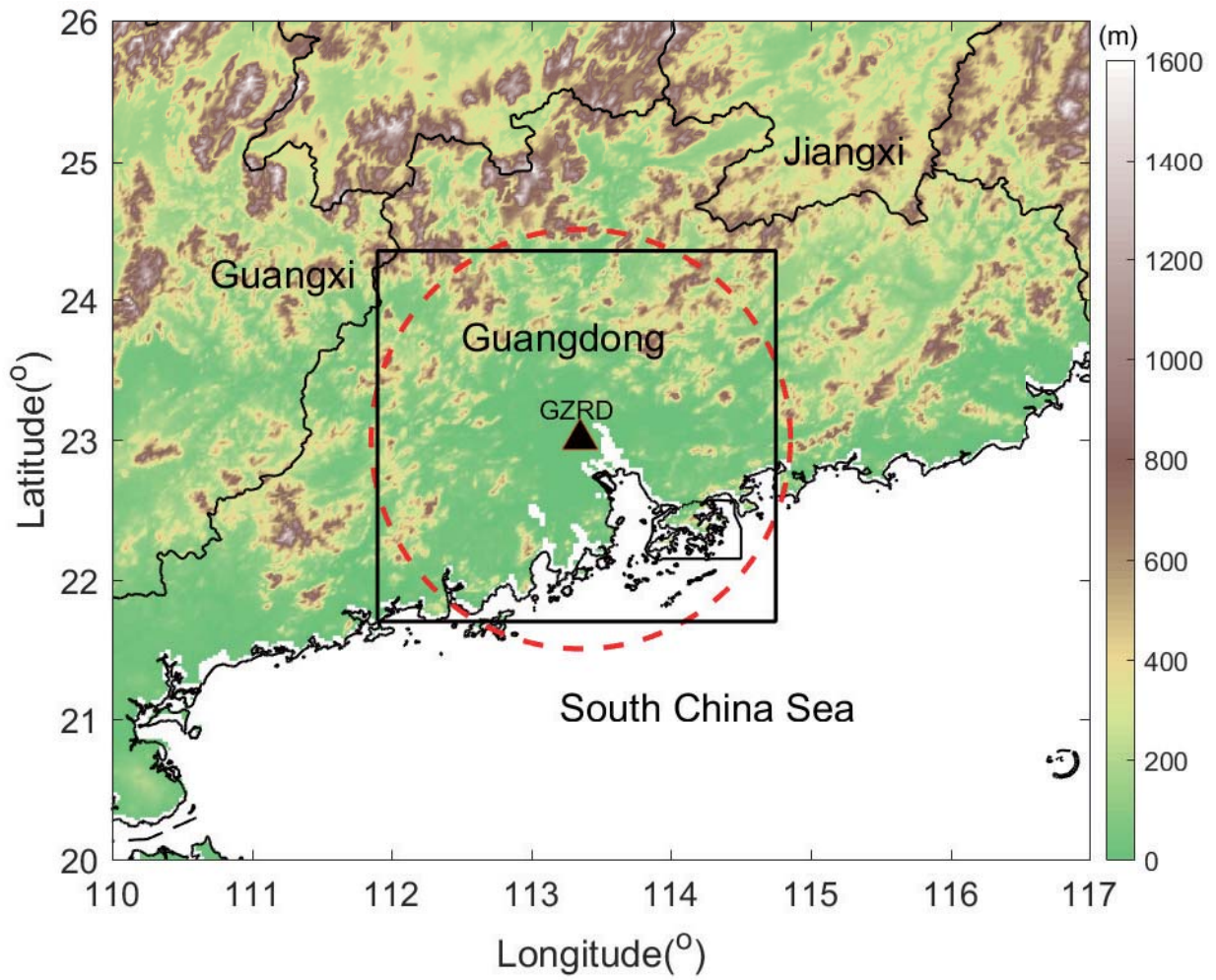


Figure 2.

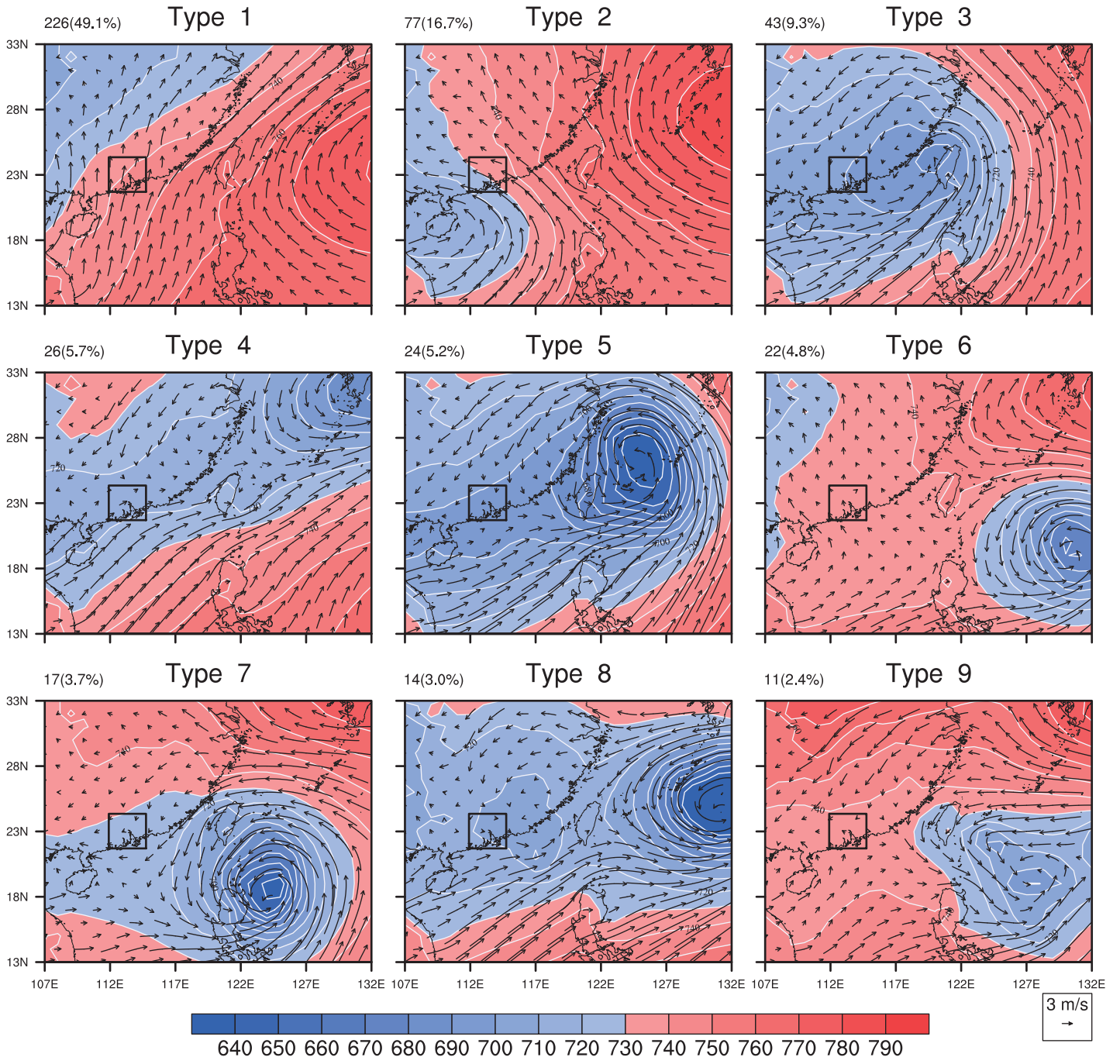


Figure 3.

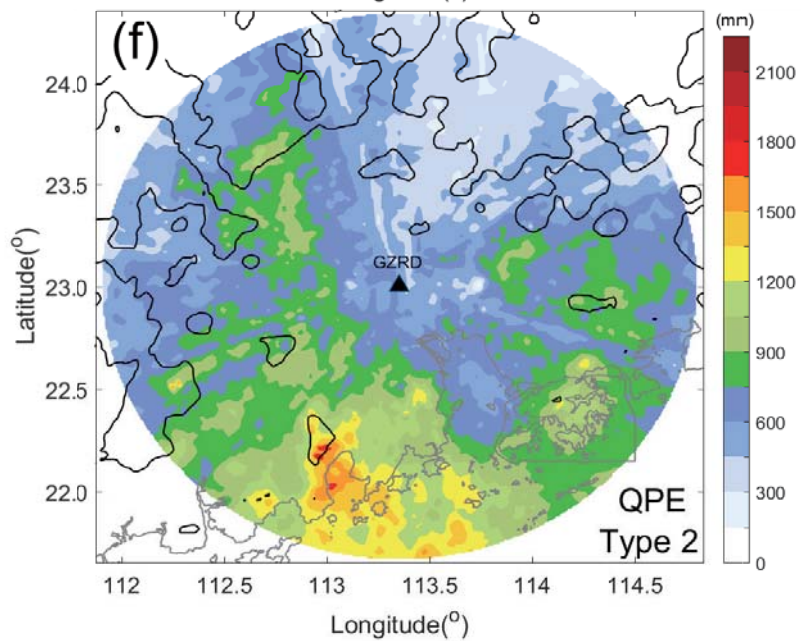
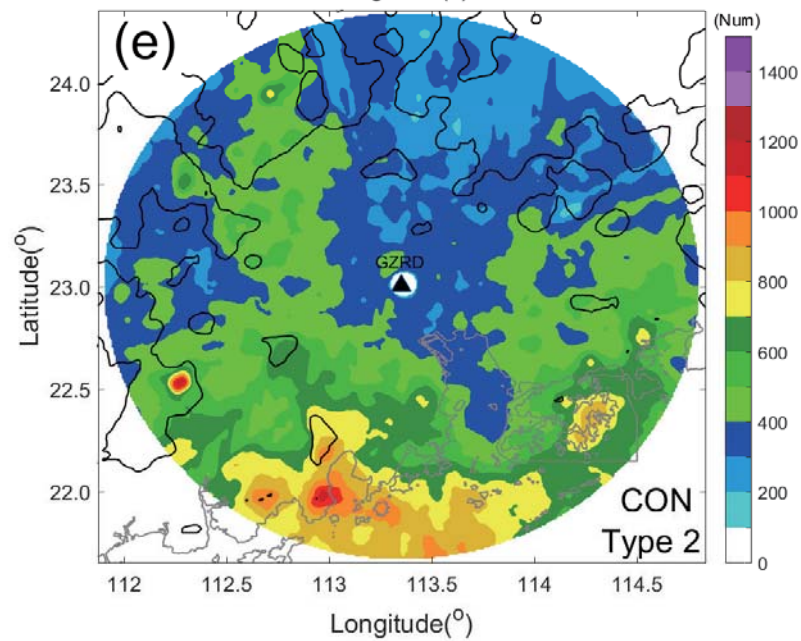
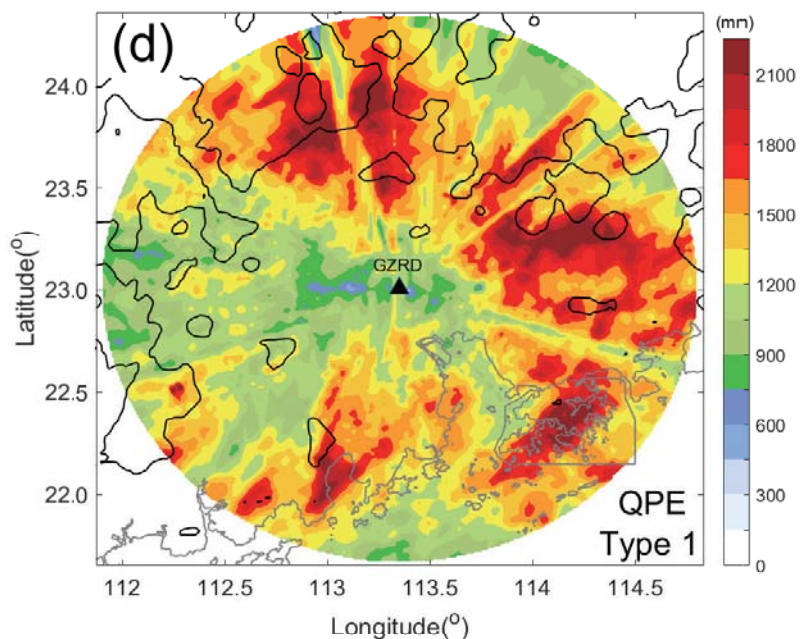
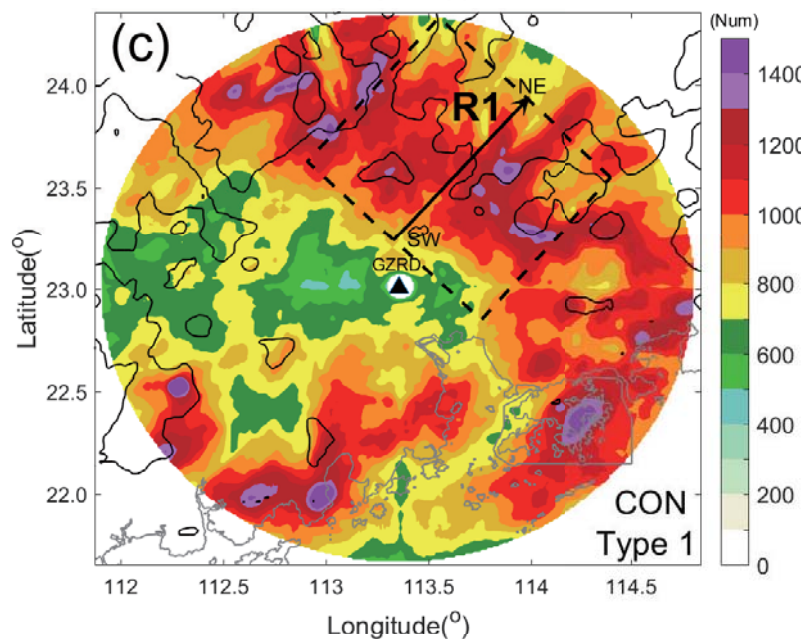
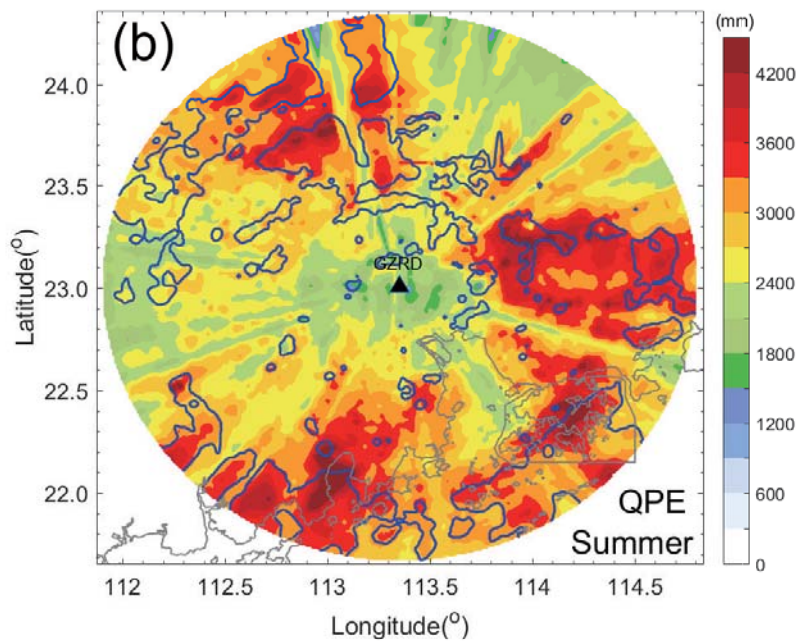
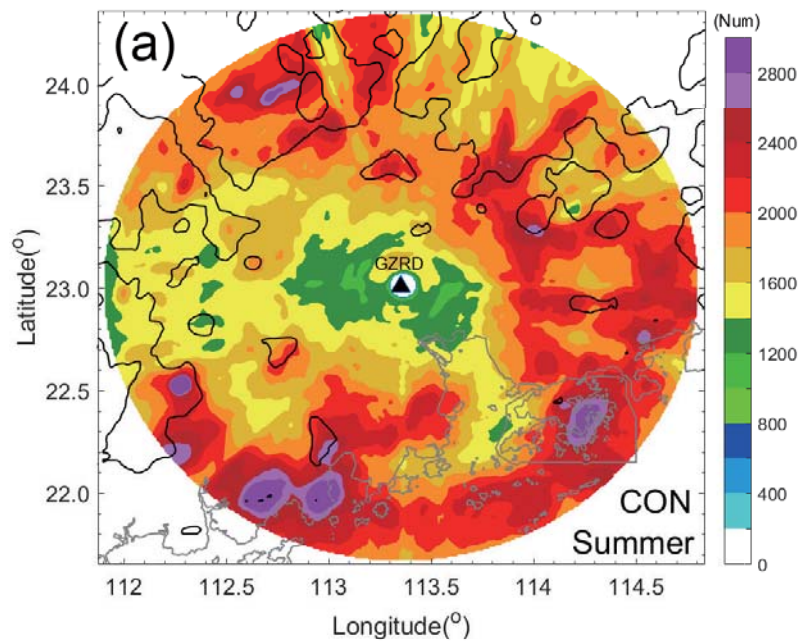


Figure 4.

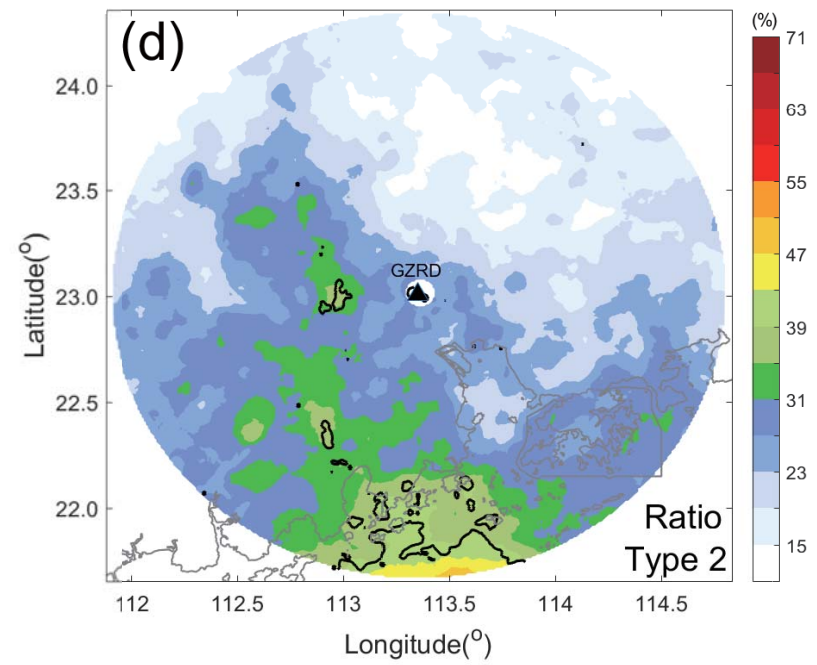
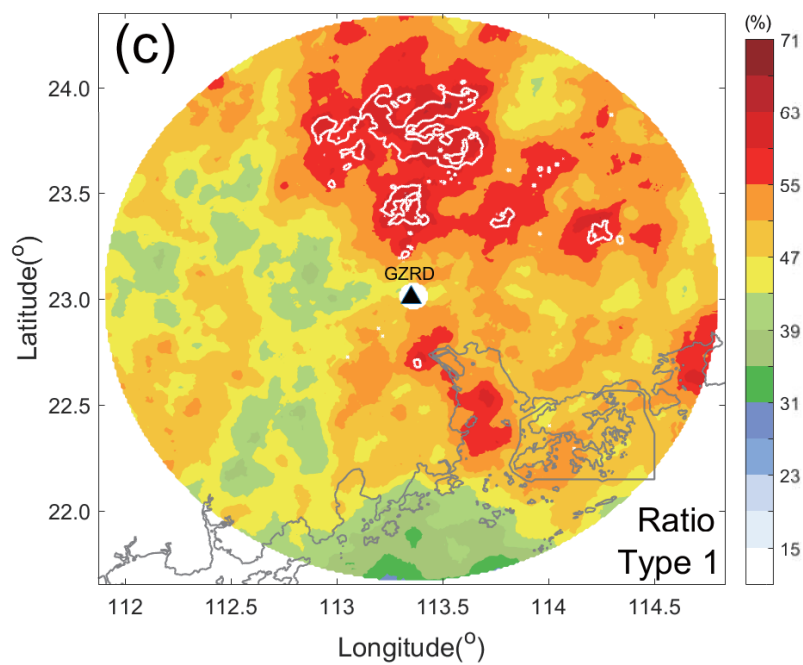
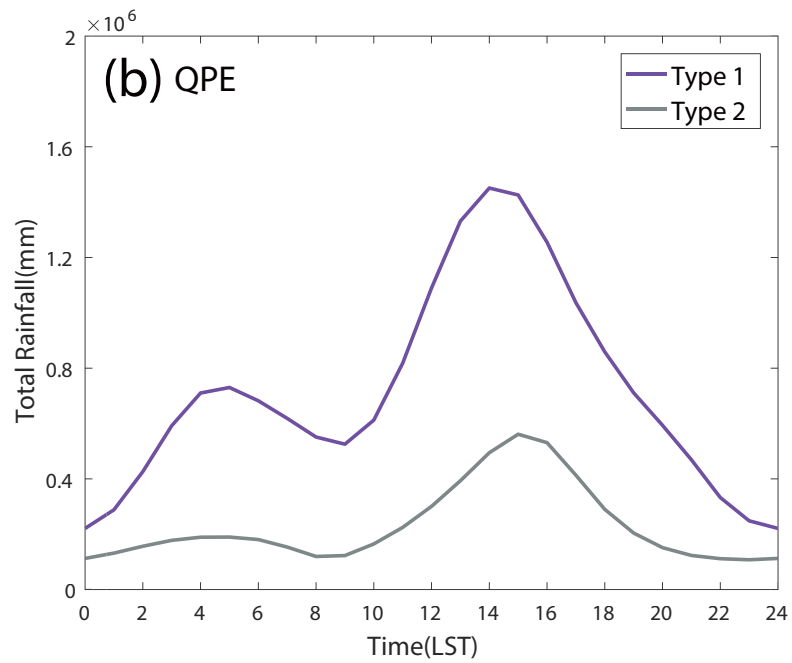
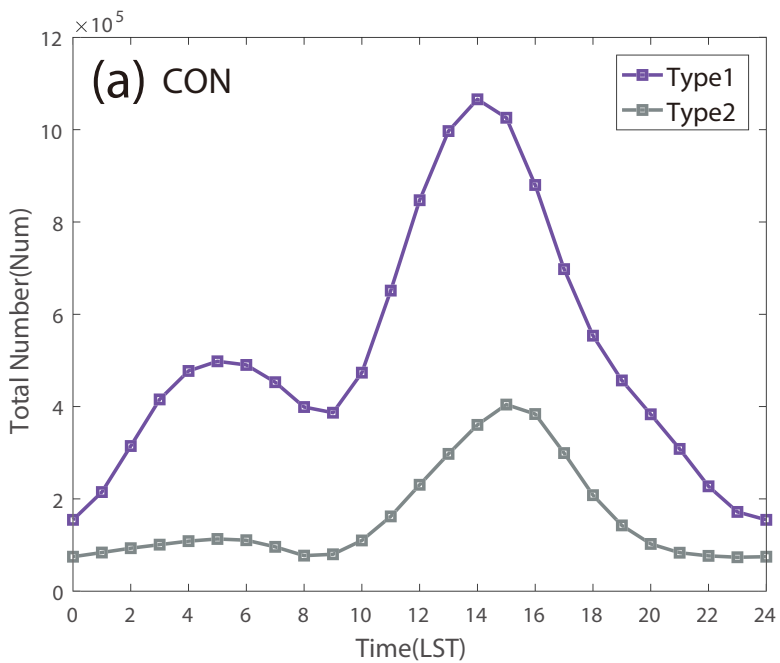


Figure 5.

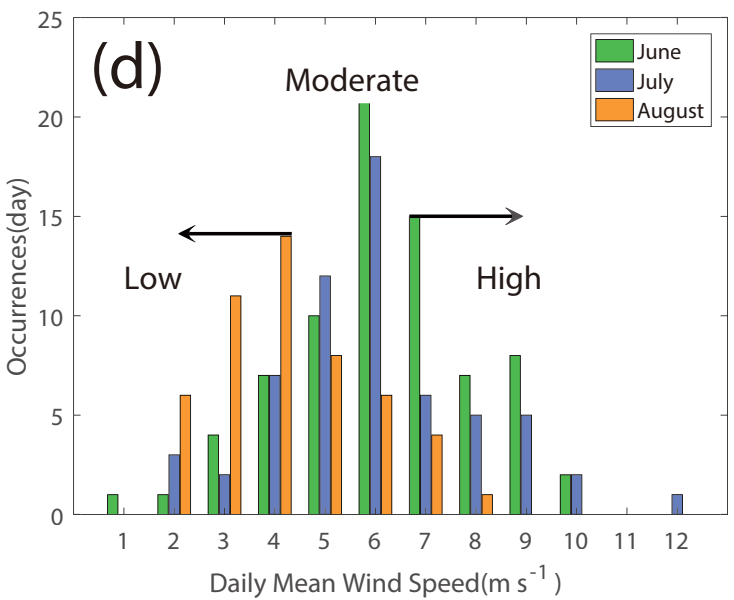
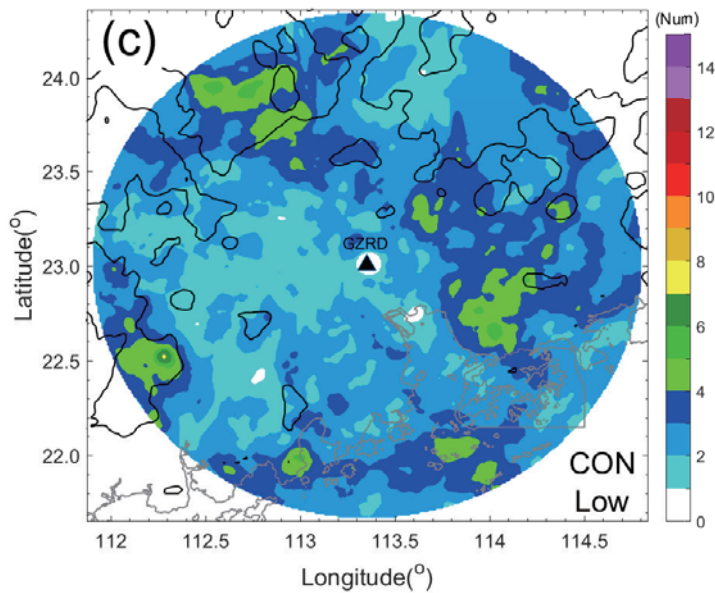
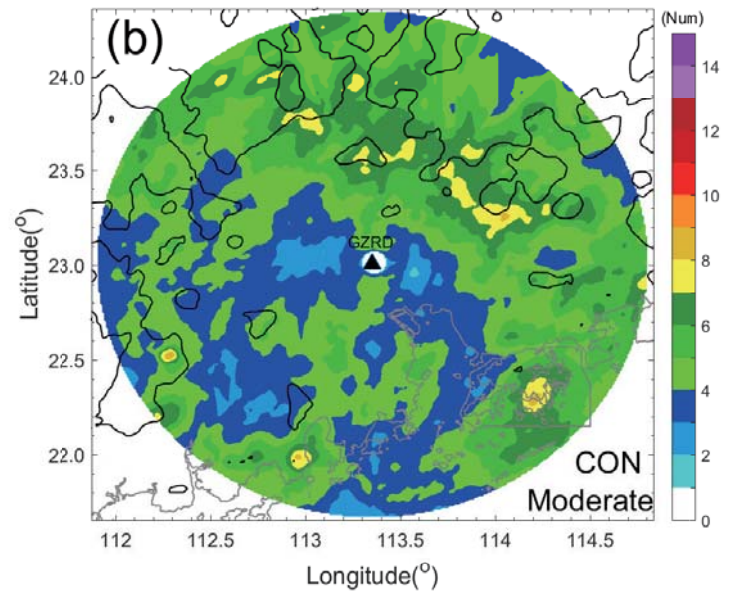
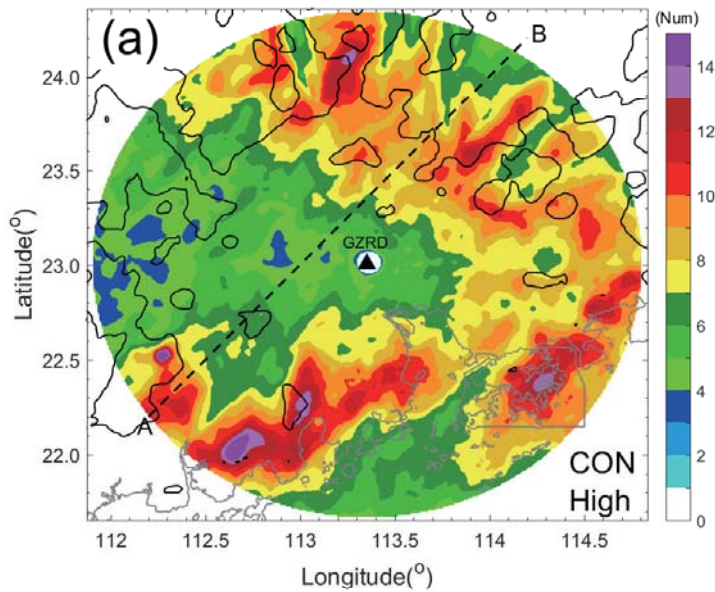


Figure 6.

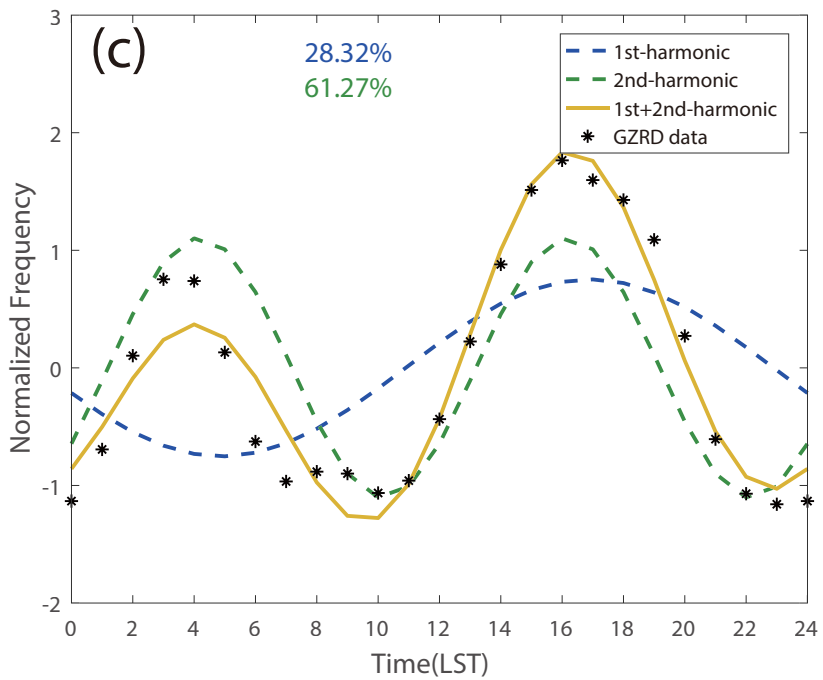
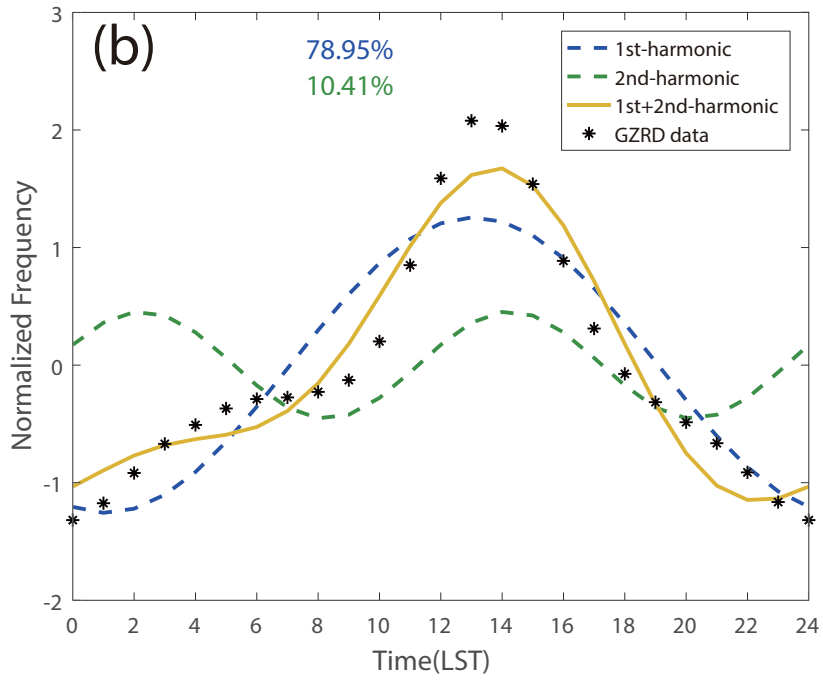
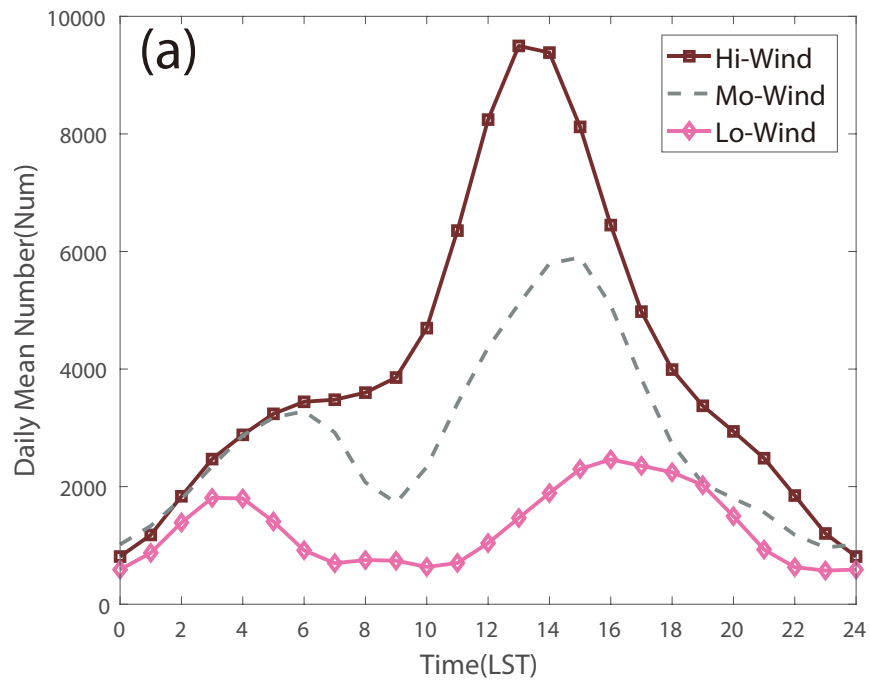


Figure 7.

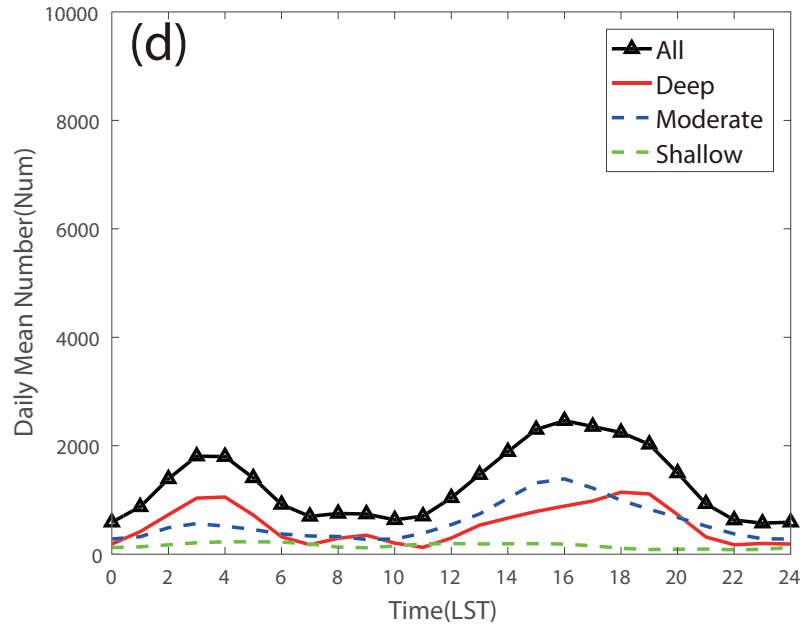
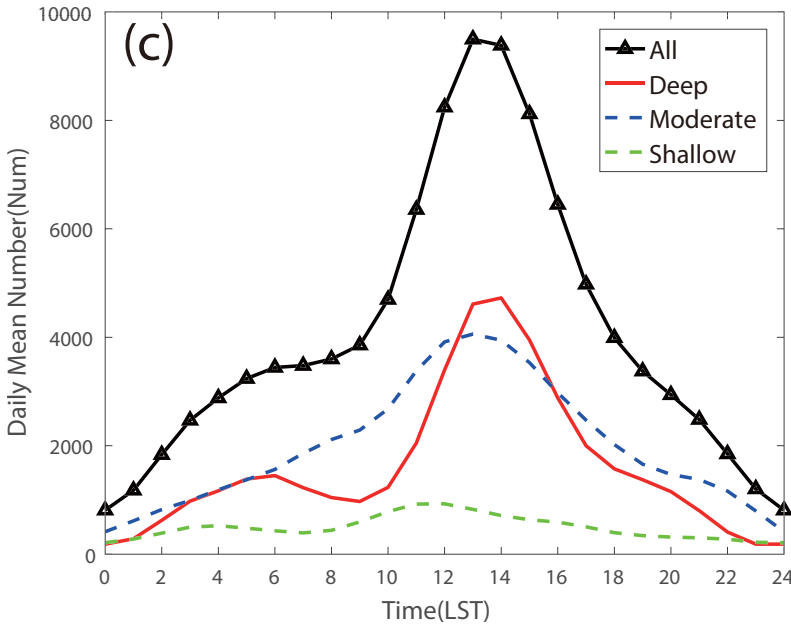
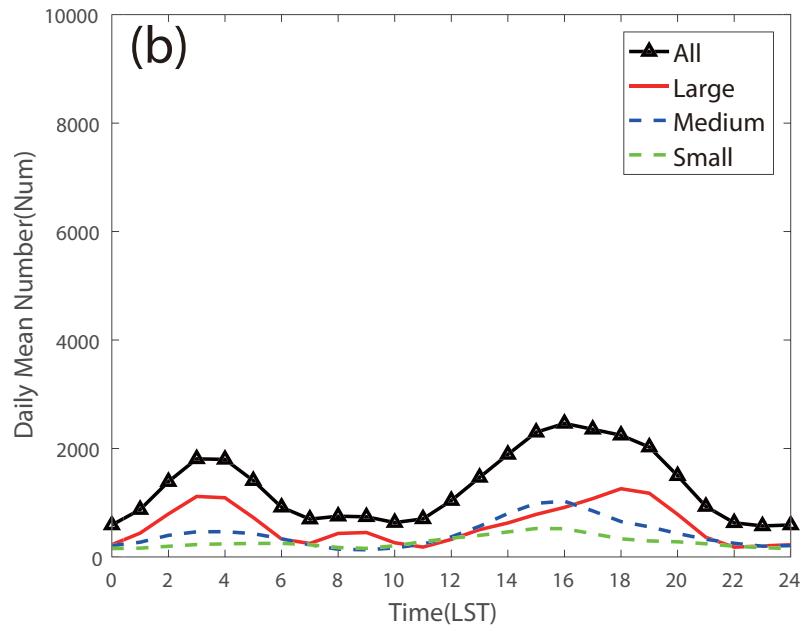
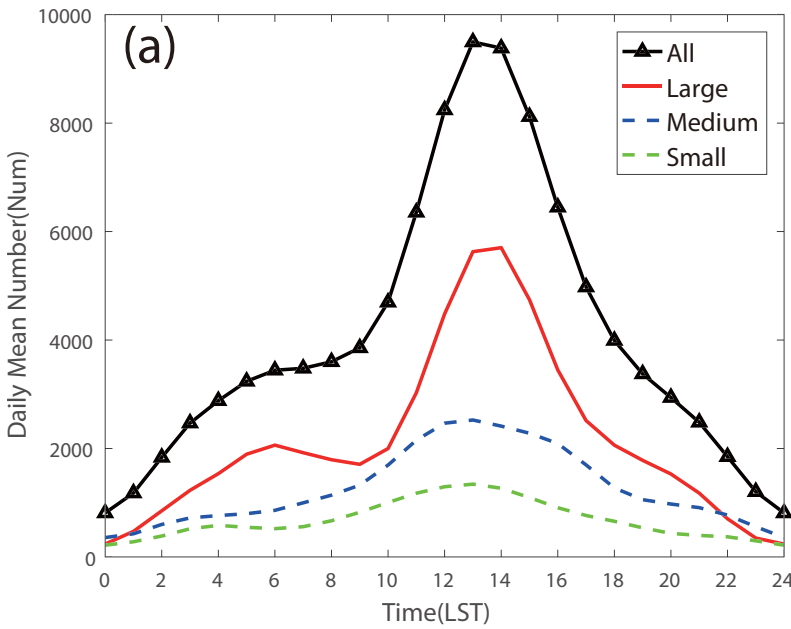


Figure 8.

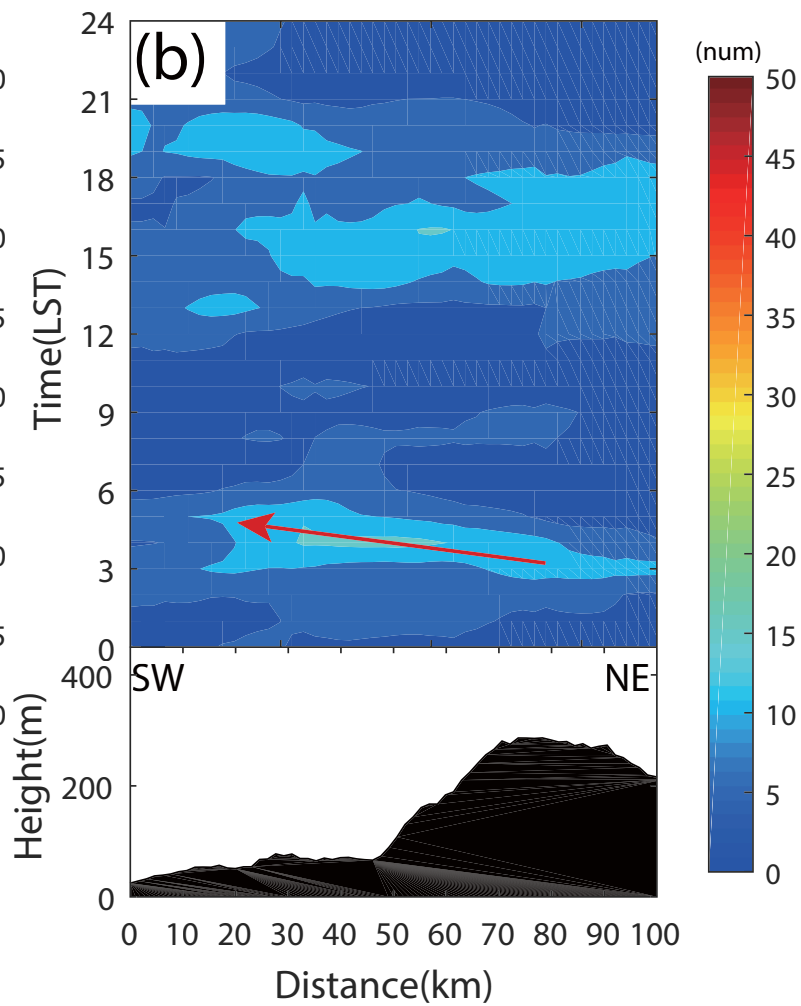
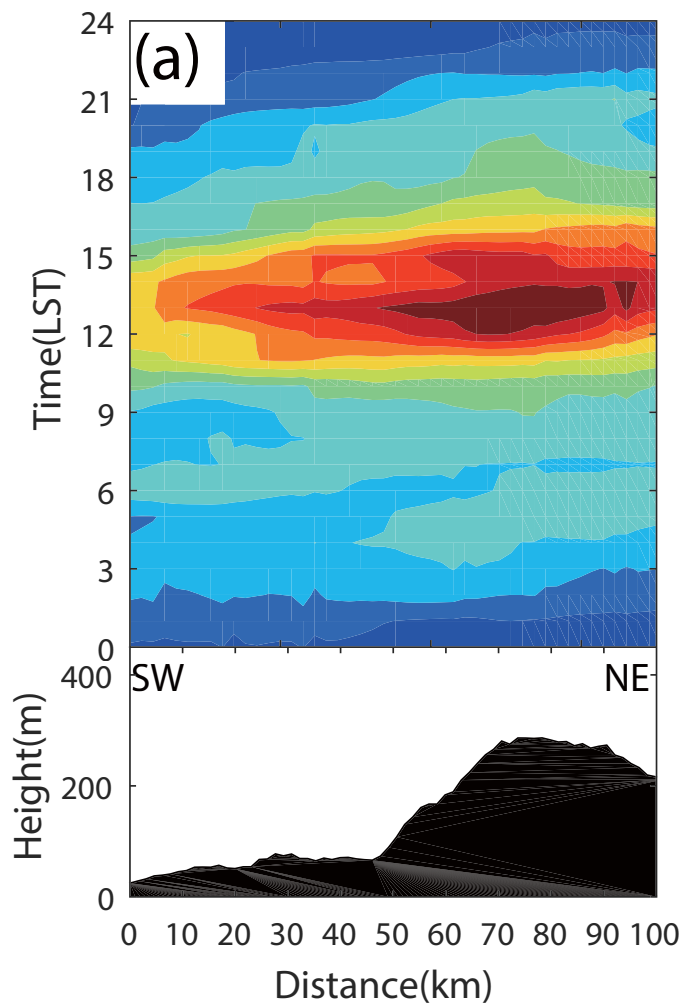


Figure 9.

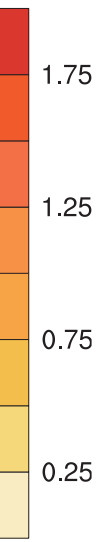
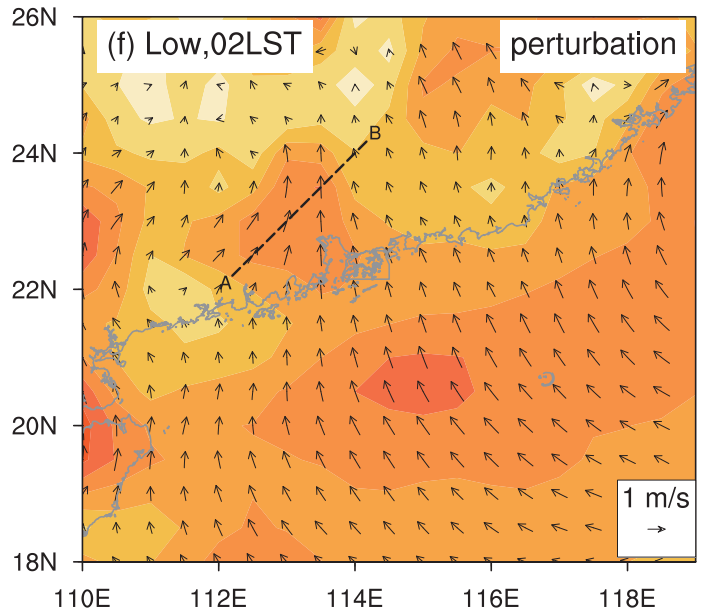
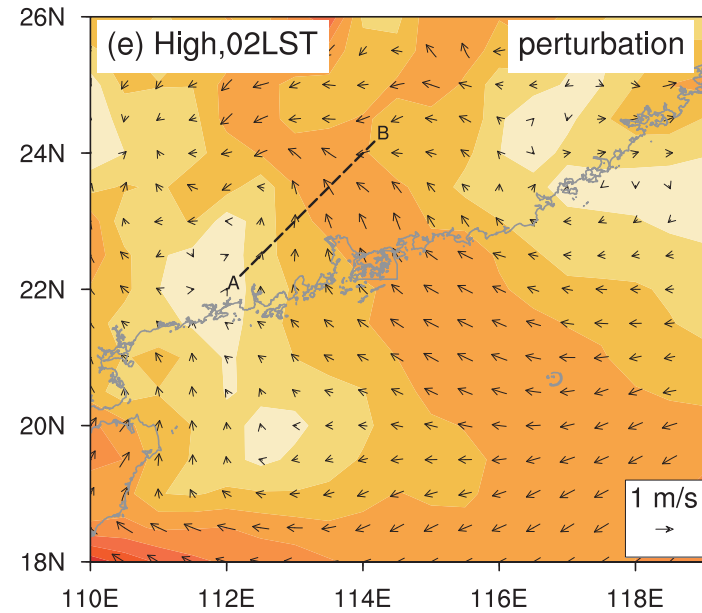
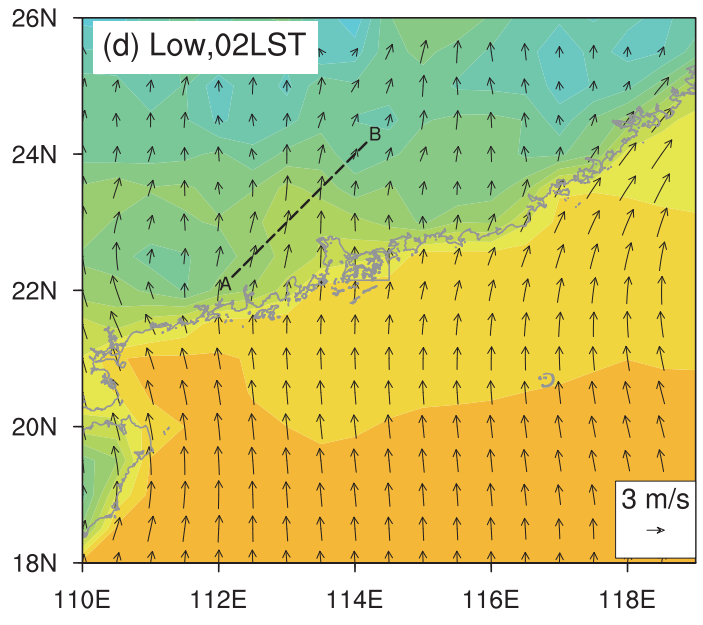
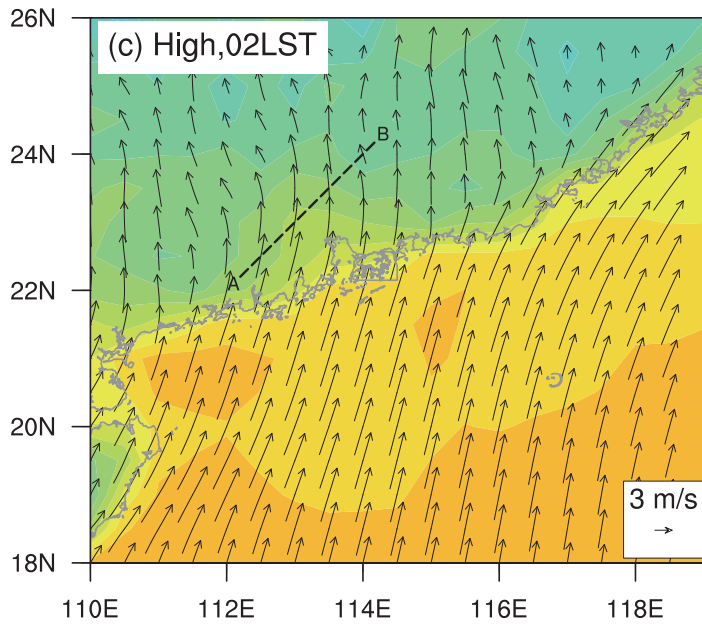
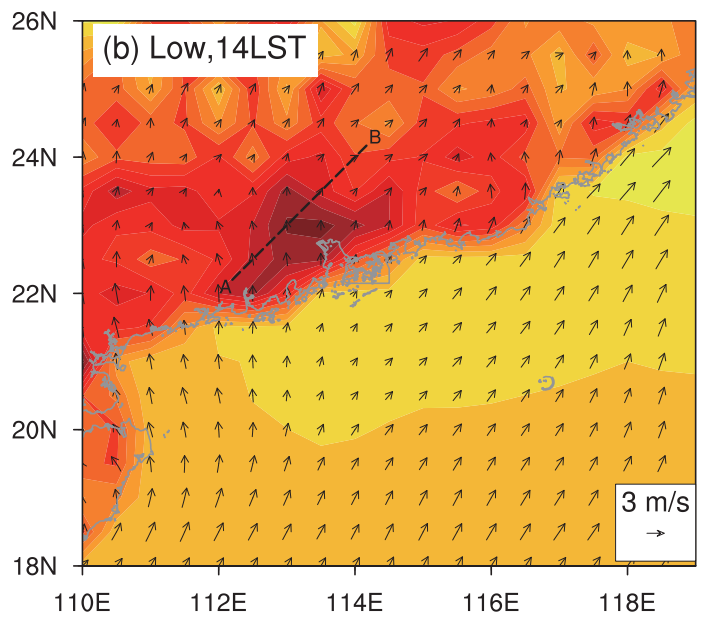
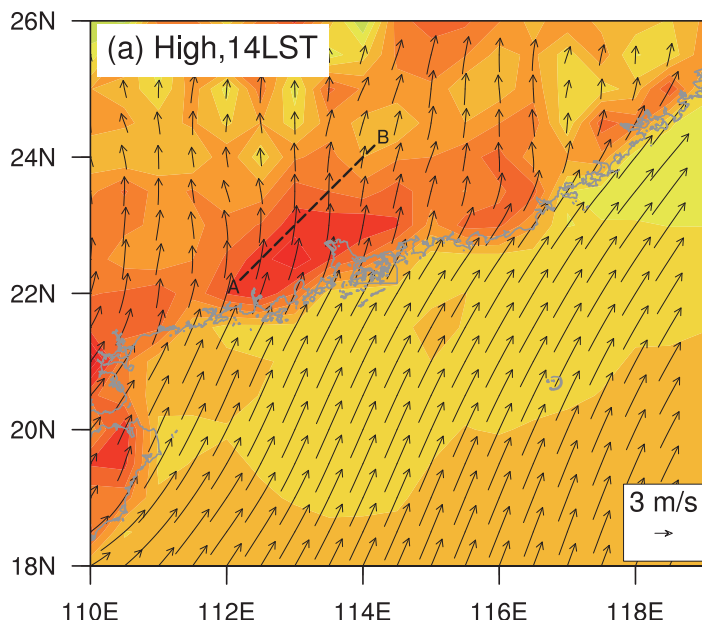
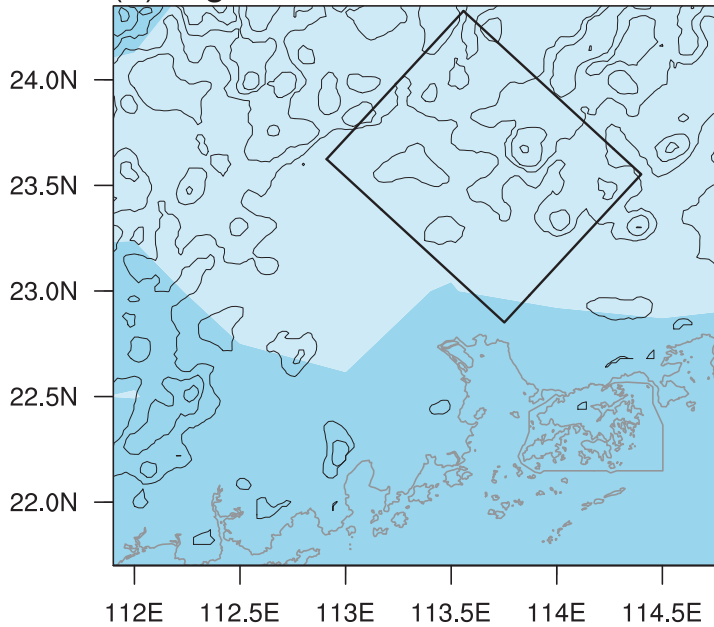
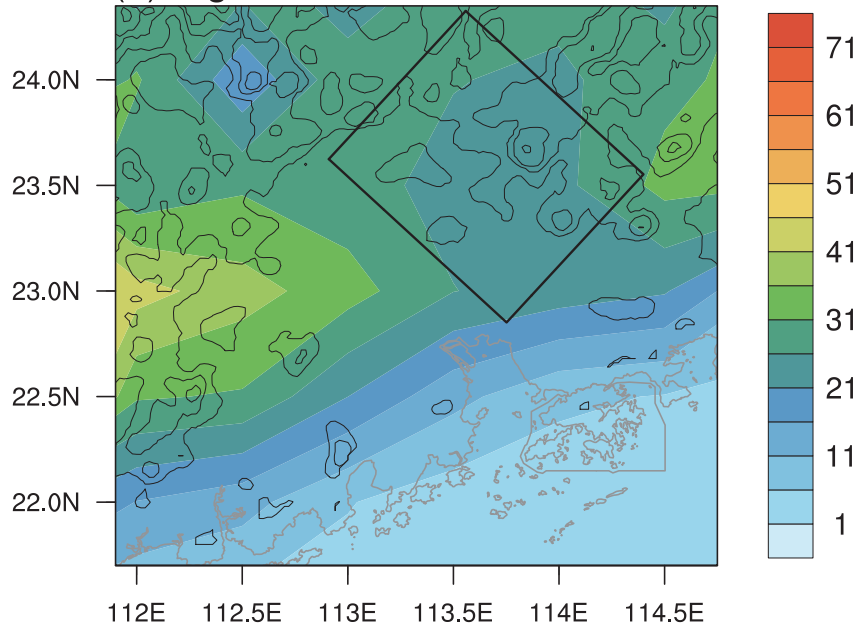


Figure 10.

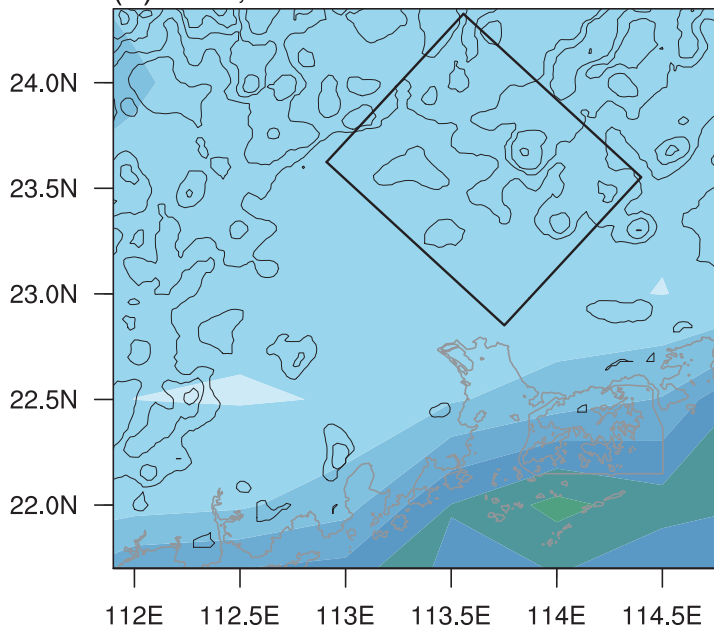
(a) High, 14LST



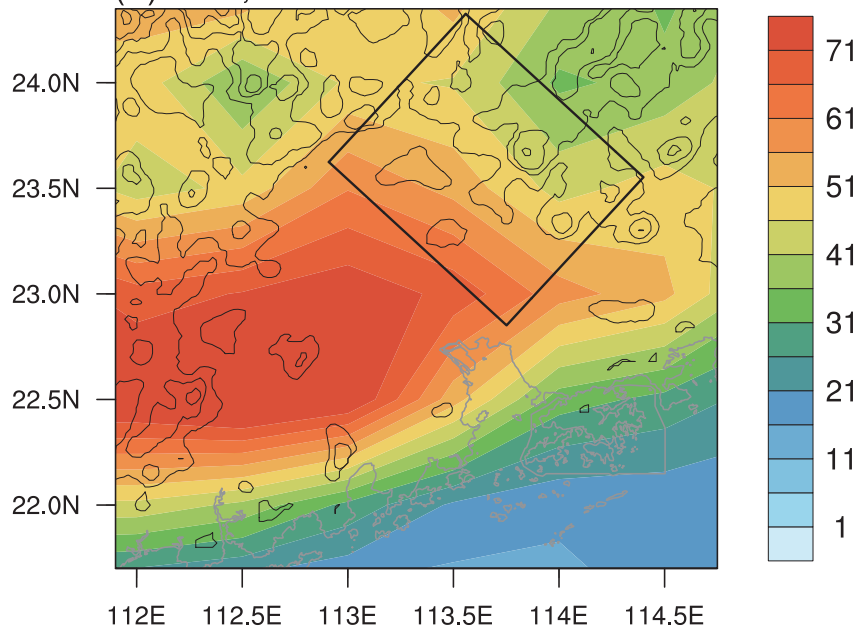
(b) High, 02LST



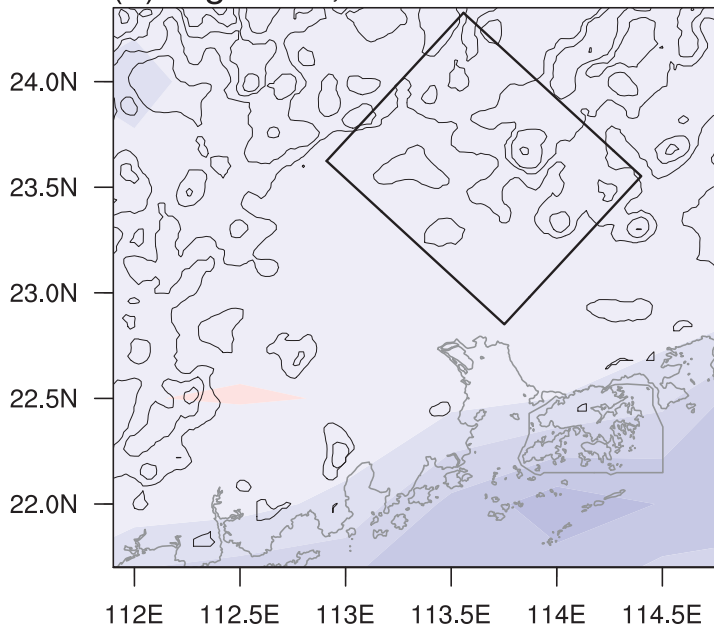
(c) Low, 14LST



(d) Low, 02LST



(e) High-Low, 14LST



(f) High-Low, 02LST

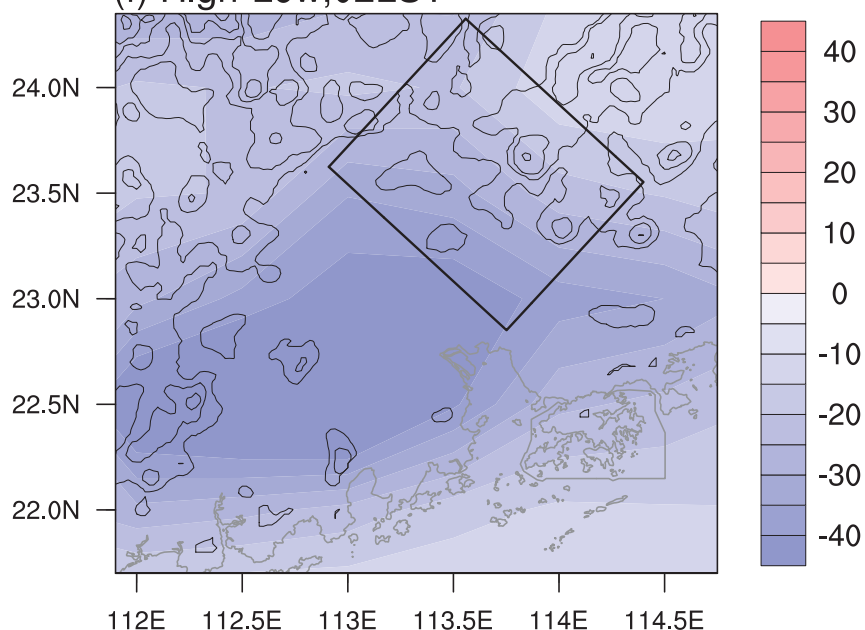
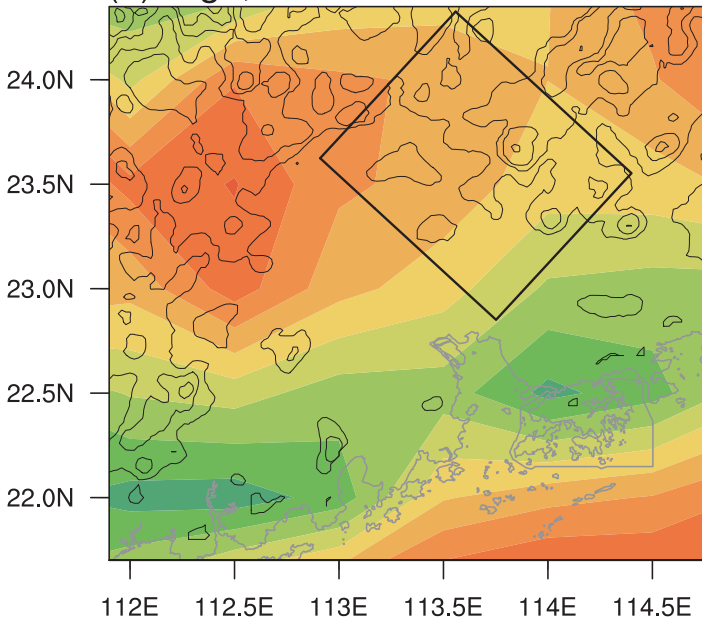
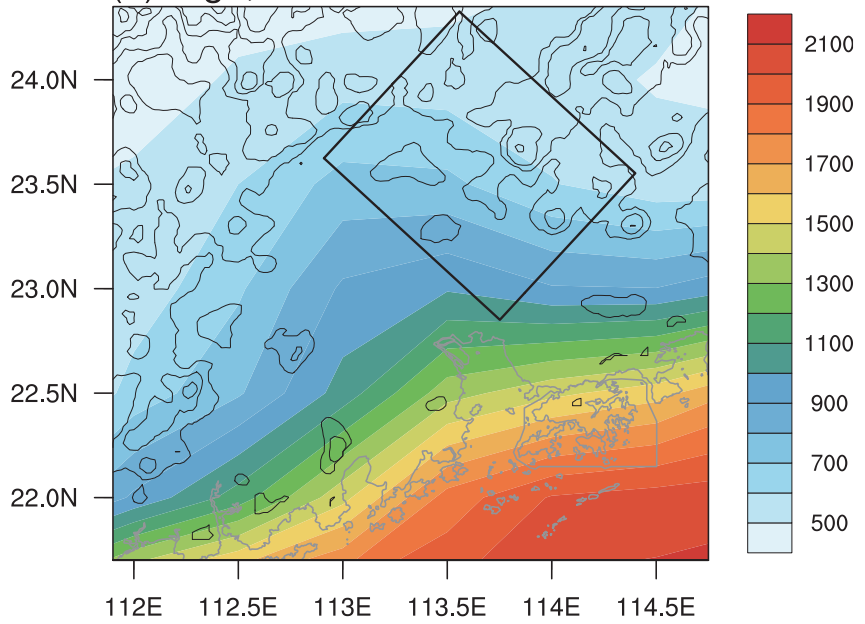


Figure 11.

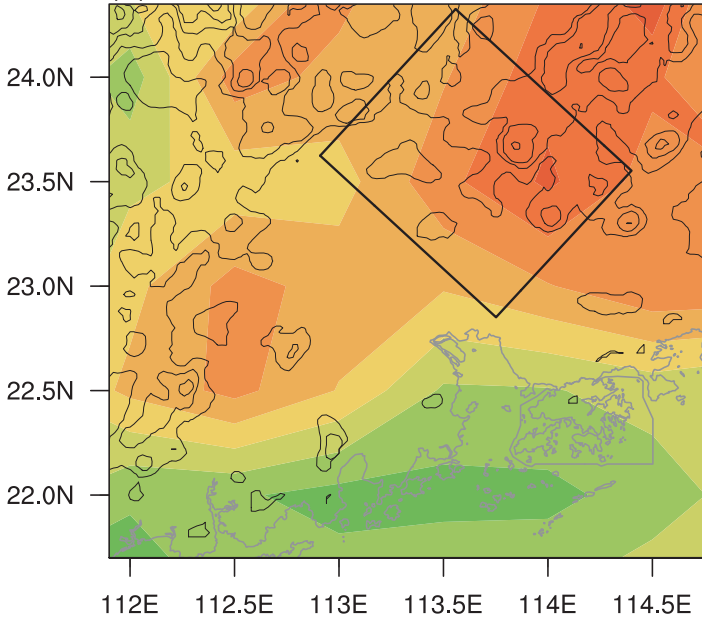
(a) High,14LST



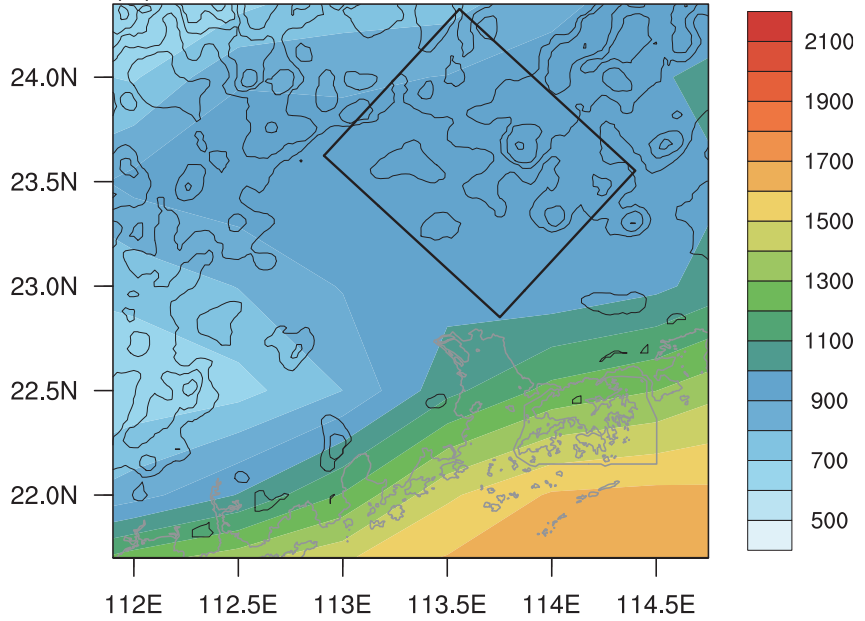
(b) High,02LST



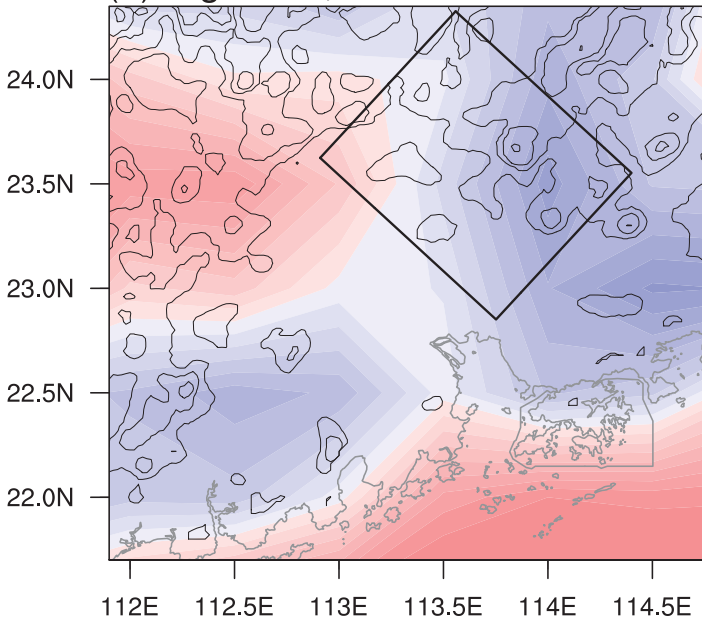
(c) Low,14LST



(d) Low,02LST



(e) High-Low,14LST



(f) High-Low,02LST

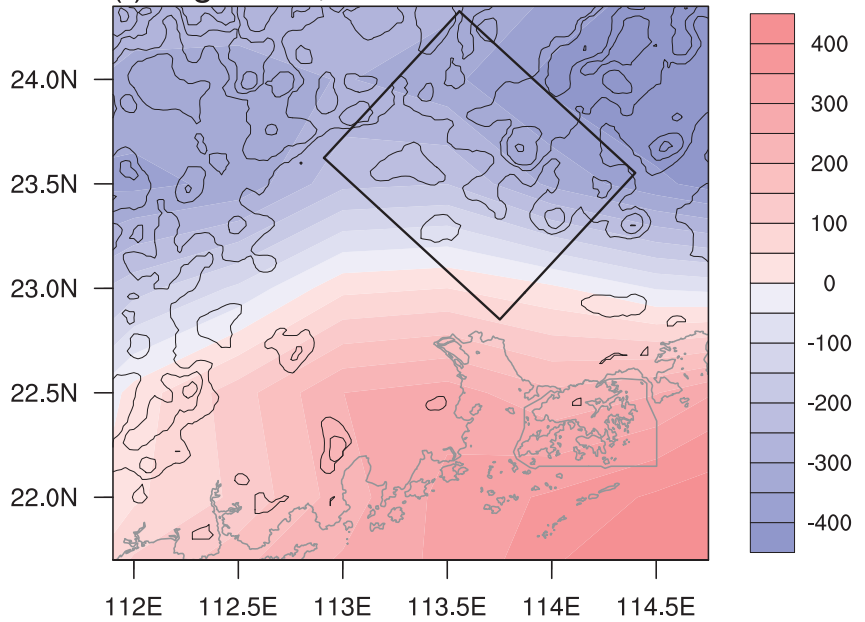


Figure 12.

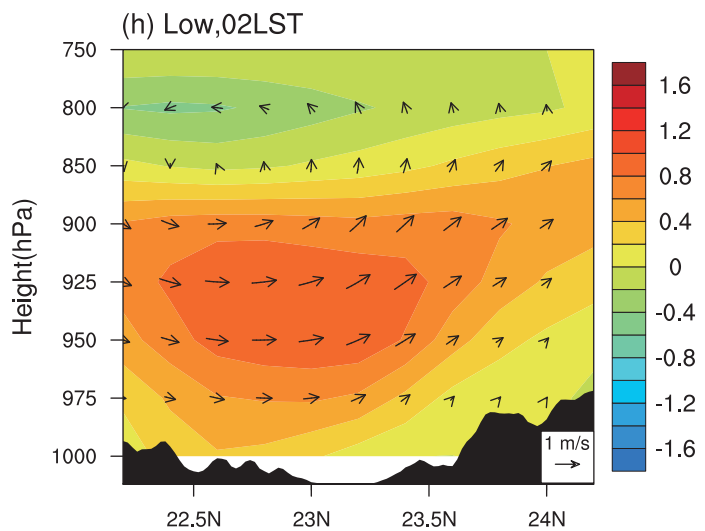
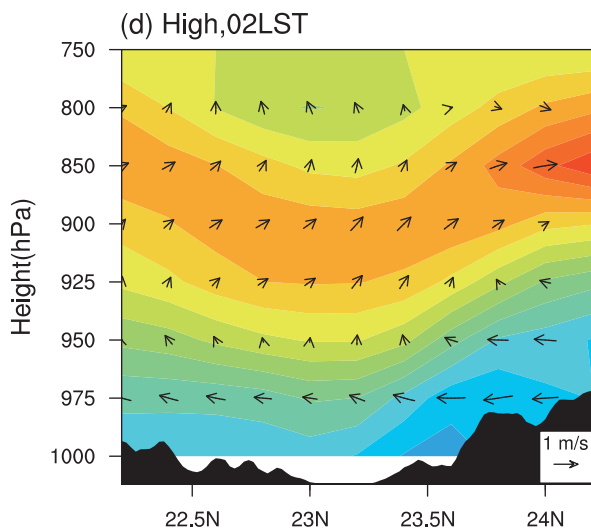
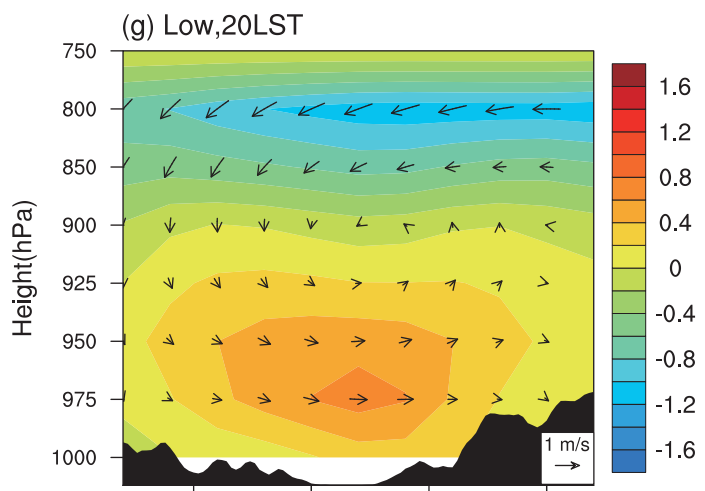
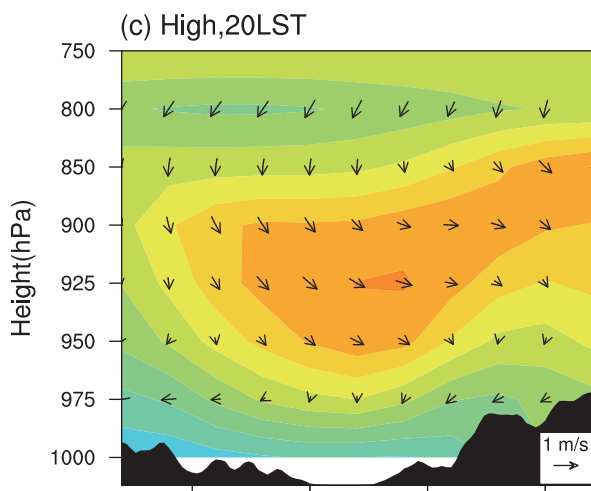
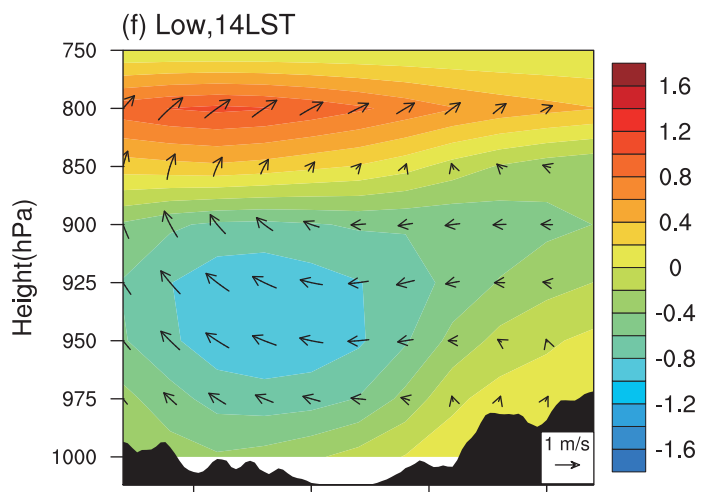
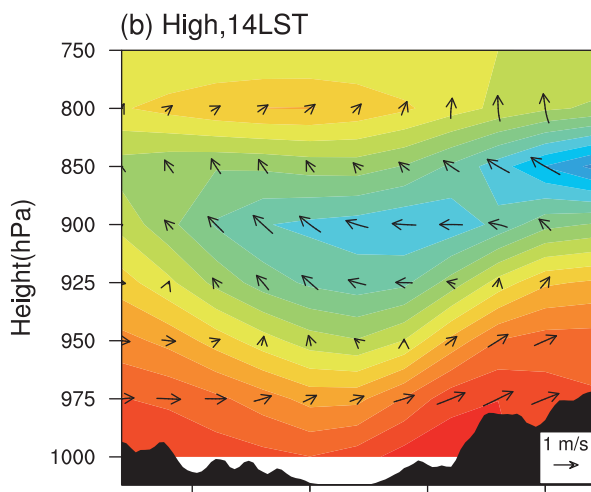
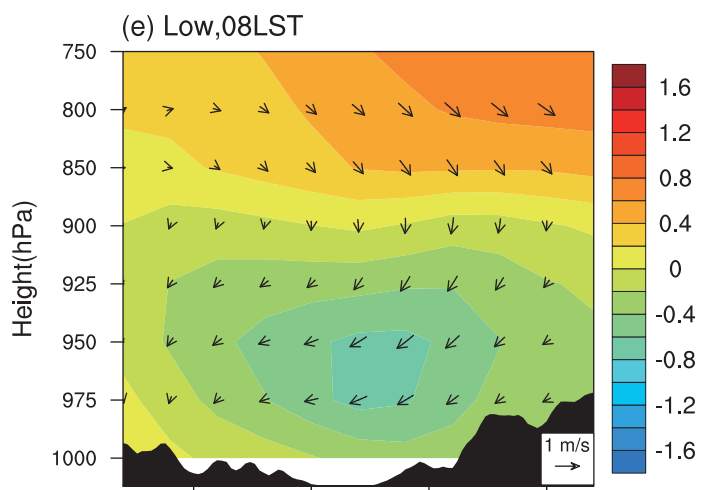
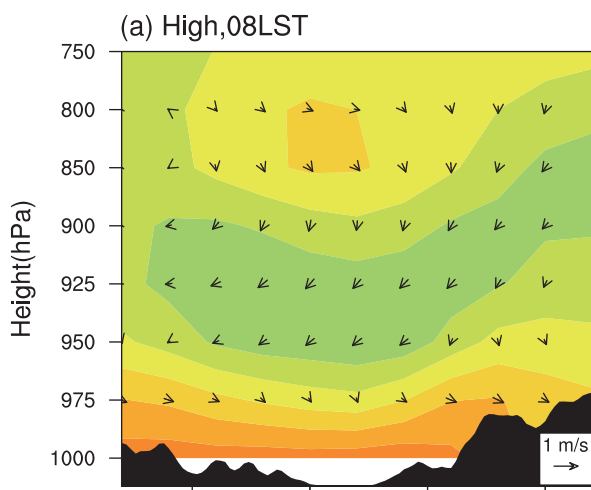


Figure 13.

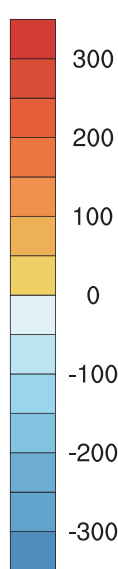
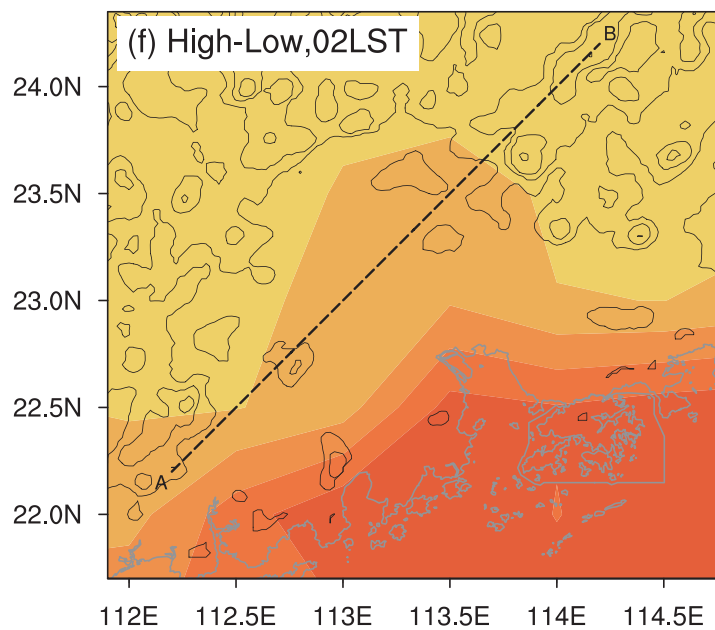
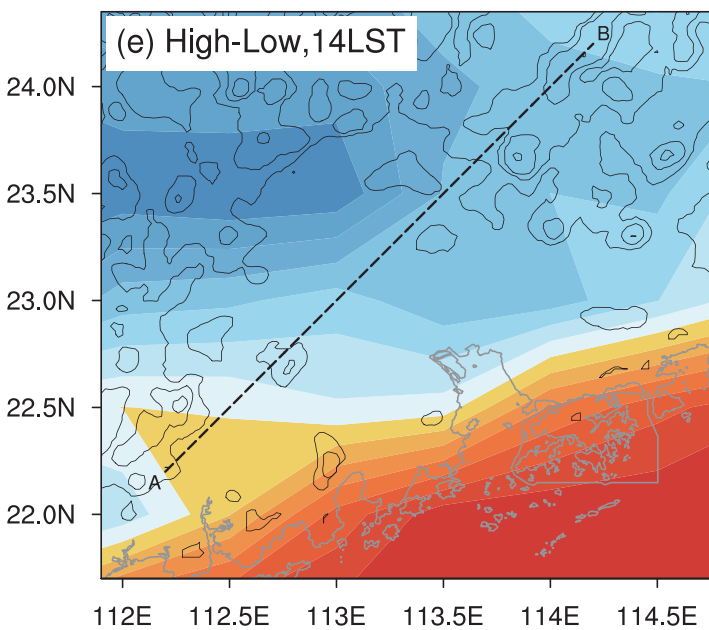
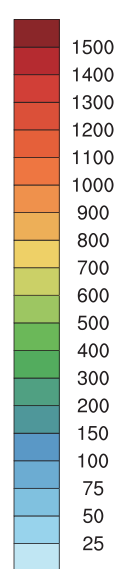
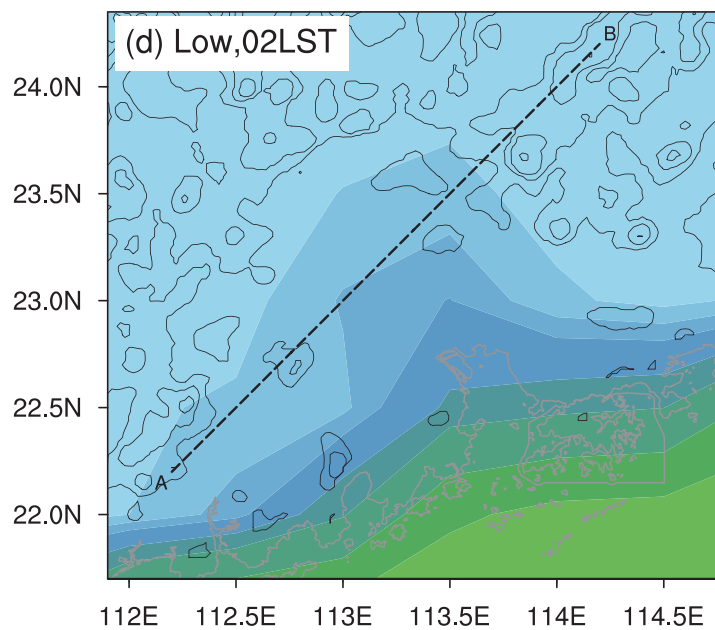
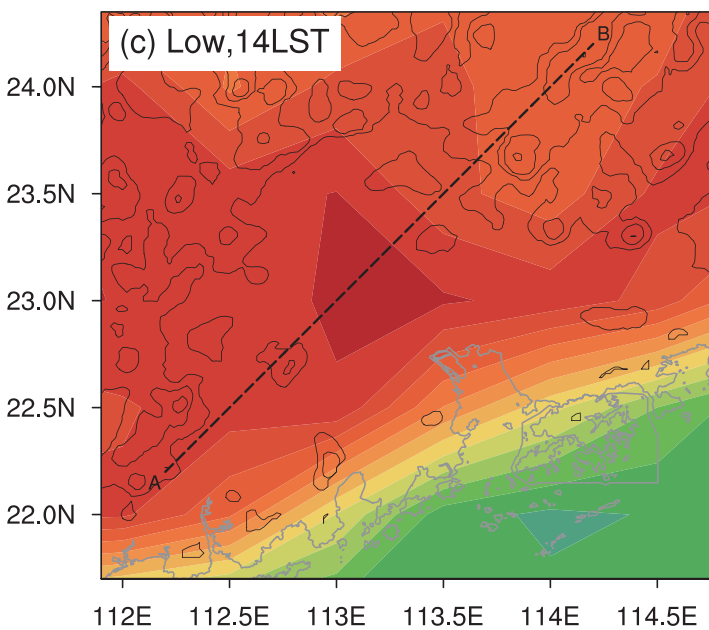
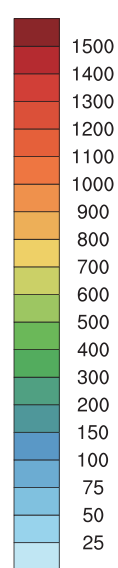
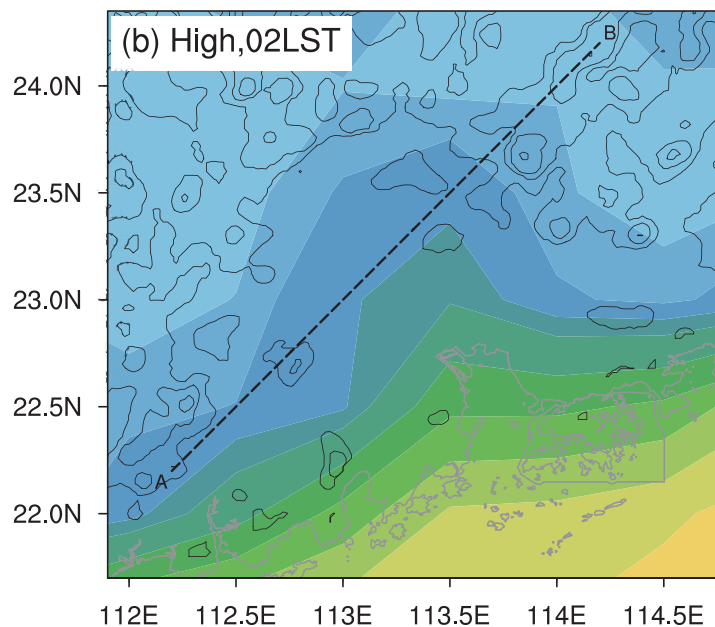
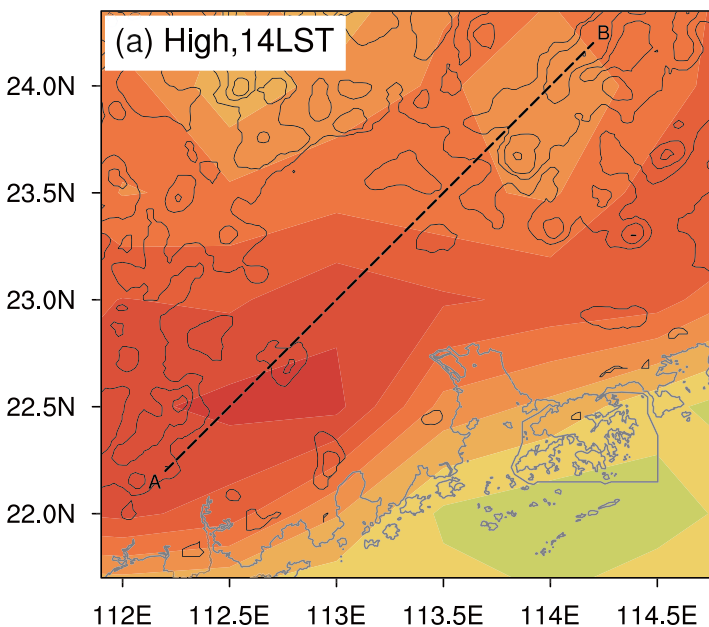


Figure 14.

